



Modeling plasmas in analytical chemistry—an example of cross-fertilization

Annemie Bogaerts¹

Received: 25 December 2019 / Revised: 24 February 2020 / Accepted: 9 March 2020 / Published online: 31 March 2020
© Springer-Verlag GmbH Germany, part of Springer Nature 2020

Abstract

This paper gives an overview of the modeling work developed in our group in the last 25 years for various plasmas used in analytical spectrochemistry, i.e., glow discharges (GDs), inductively coupled plasmas (ICPs), and laser ablation (LA) for sample introduction in the ICP and for laser-induced breakdown spectroscopy (LIBS). The modeling approaches are briefly presented, which are different for each case, and some characteristic results are illustrated. These plasmas are used not only in analytical chemistry but also in other applications, and the insights obtained in these other fields were quite helpful for us to develop models for the analytical plasmas. Likewise, there is now a huge interest in plasma–liquid interaction, atmospheric pressure glow discharges (APGDs), and dielectric barrier discharges (DBDs) for environmental, medical, and materials applications of plasmas. The insights obtained in these fields are also very relevant for ambient desorption/ionization sources and for liquid sampling, which are nowadays very popular in analytical chemistry, and they could be very helpful in developing models for these sources as well.

Keywords Modeling · Plasma · Glow discharge · Inductively coupled plasma · Laser ablation · Plasma–liquid interaction

Introduction

Various analytical methods are based on plasmas for material sampling. The most widely used is the inductively coupled plasma (ICP), used for mass spectrometry (MS) and optical emission spectrometry (OES) [1–3], but also laser ablation (LA), either as a sampling method for ICP-MS and ICP-OES [4–7] or for laser-induced breakdown spectrometry (LIBS) [8–10], and glow discharges (GD) in combination with MS or OES [11–14] have been quite popular for many years.

For good analytical performance of these sources, a thorough insight into their underlying mechanisms is beneficial. This insight can be obtained by experiments (plasma diagnostics), but measurements inside the plasma are often difficult, due to the small dimensions and because of possible

disturbance of the processes, affecting the measurement outcome. Therefore, computer modeling of the plasma processes can also provide valuable insights.

In the last 25 years, we developed computer models for various plasmas used in analytical spectrochemistry, including GDs, ICPs, LA, and LIBS. In this feature article, an overview is given of this modeling work. The modeling approaches used in each case are briefly explained, as they are different for the different types of plasmas, and some characteristic results are shown. In developing these models, we based ourselves on models developed for other plasma application fields, like materials science and the semiconductor industry, where similar plasmas are being used, although this is not always very well known in the analytical chemistry community.

Such cross-fertilization between different fields can indeed be very helpful, and can also be relevant for other gas and liquid sampling sources in analytical spectrometry, which have become very popular in recent years, such as the various ambient desorption/ionization sources [15–18]. Indeed, atmospheric pressure non-thermal plasmas, such as dielectric barrier discharges (DBDs), atmospheric pressure glow discharges (APGDs), and plasma jets, are widely used for many environmental, medical, and materials science applications, and the

Published in the topical collection featuring *Female Role Models in Analytical Chemistry*.

✉ Annemie Bogaerts
annemie.bogaerts@uantwerpen.be

¹ Research group PLASMANT, Department of Chemistry, University of Antwerp, Universiteitsplein 1, 2610 Wilrijk, Antwerp, Belgium

insights obtained in these fields can be very helpful for gas sampling sources in analytical chemistry as well. Likewise, liquid sampling sources in analytical chemistry (e.g., [19–21]) can benefit from the knowledge gained from plasma–liquid interactions used for many other applications, like in medicine, water treatment, and materials science (e.g., nanoparticle synthesis). This article can hopefully inspire analytical chemists to learn from these other fields, for better insight in these gas and liquid sampling analytical sources as well.

Modeling of glow discharges

Modeling approaches

Glow discharges (GDs) used in GDMS and GD-OES typically operate at reduced pressure and are far from thermodynamic equilibrium. This means that the electrons have a much higher temperature than the other plasma species, and must be described separately, with a non-equilibrium modeling approach.

There exist several modeling approaches to describe non-equilibrium plasmas such as GDs, each with its own benefits and limitations. The simplest modeling approach is an analytical model, which is based on simple analytical formulas to make some general and quick predictions on the plasma behavior. However, it is only valid under certain—very limited and simplified—conditions. Numerical modeling approaches are more powerful. They range from simple, fast models to very complicated and time-consuming models.

Chemical kinetics models solve mass conservation equations for the various plasma species, with source and loss terms as defined by the chemical reactions in the plasma. They are very fast, and therefore suitable to describe a detailed plasma chemistry, but they typically do not account for spatial variations (so-called 0D approach), which is a clear limitation.

Fluid models also solve mass conservation equations for the various plasma species, but in addition, they also solve transport equations, based on diffusion (due to concentration gradients), migration under the influence of the electric field (only for charged species), and sometimes convection (due to the gas flow). Hence, they are more powerful, while still being time-efficient, and can be described in 1D, 2D, or even 3D, although the latter would require considerable calculation time. Therefore, 2D fluid models are more common, as many plasma sources can be approximated with cylindrical symmetry. Fluid models typically also solve Poisson's equation for a self-consistent calculation of the electric field distribution in the plasma, based on the charged species density profiles. A disadvantage of a fluid modeling approach is that it assumes that the plasma species are more or less in equilibrium with the electric field, i.e., the energy gained by the species from the

electric field is more or less balanced by the energy lost due to collisions. While this may be appropriate for ions and electrons in the bulk plasma (or negative glow region, characterized by a weak electric field), and of course for neutral species (which do not gain energy from the electric field at all), electrons in the sheaths in front of the electrodes (or the cathode dark space, CDS) typically gain much more energy from the strong electric fields in these regions than they lose by collisions. Therefore, other modeling approaches are needed to describe the non-equilibrium behavior of electrons.

One approach to account for the electron non-equilibrium behavior is solving the Boltzmann transport equation, which solves the full electron energy distribution function. However, this method can be mathematically complex, certainly in more dimensions and for complex geometries. An easier method from a mathematical point of view is to apply Monte Carlo simulations, which describe the electrons at the lowest microscopic level, i.e., as individual particles or super-particles (with a certain weight, corresponding to the real number of electrons they represent). The trajectory of the electrons during successive time-steps is described by Newton's laws, and the probability of collisions during that time-step is described, based on the collision cross sections, the number density of the collision partners and the traveled distance. This collision probability yields a number between 0 and 1. It will be compared with a random number between 0 and 1, and if the probability is lower, no collision occurs, and the electron is followed during the next time-step. If the probability is higher, a collision takes place, and the kind of collision, as well as the new energy and direction after collision, can also be determined by random numbers. By following in this way a large number of electrons during successive time-steps, their behavior can be statistically and accurately described. This method can also be used for other plasma species that are not in equilibrium with the electric field, such as ions in the CDS (see below). While this method is very accurate, it requires a longer calculation time than a fluid model, because a large number of plasma species must be simulated for statistically valid results. Moreover, this method is not self-consistent, because it requires the electric field distribution as input in the model. The latter limitation can be overcome in so-called particle-in-cell–Monte Carlo collision (PIC-MCC) simulations, which use the same approach as the above Monte Carlo model, typically for both ions and electrons, but in addition, the electric field is calculated with Poisson's equation, from the species positions (determining a space charge distribution). This method is the most accurate approach, and it is self-consistent, but it requires an even longer calculation time.

Hence, it is clear that each model has its advantages and limitations. A smart approach is therefore to combine various models, for the various plasma species, in a so-called hybrid model. The energetic plasma species, like electrons, which are not in equilibrium with the electric field, can then be simulated

with a Monte Carlo approach, while for the slower ions and neutral species, a fluid model is appropriate, to save calculation time and to provide a self-consistent calculation.

For this reason, we developed a hybrid Monte Carlo (MC)–fluid model, to describe the behavior of electrons, argon (Ar^+) ions and energetic Ar atoms in the GD plasma [22–25]. The (energetic) electrons are described with a MC approach [22], as explained above. Once the electrons have lost most of their energy by inelastic collisions with the Ar atoms, they are not really important as “energetic electrons” anymore, as they cannot cause any further excitation and ionization of the Ar atoms, and their main role is to carry the electric current and to provide negative space charge. This can as well be described in a fluid approach [23], which is less computationally intensive, as explained above. This fluid model describes the “slow” electrons as a group, as well as the ions, based on mass conservation equations and transport equations, coupled to Poisson’s equation for a self-consistent electric field calculation, as explained above.

Finally, the ions are accelerated by the strong electric field in the CDS in front of the cathode, and they give rise to cathode sputtering, releasing the material to be analyzed into the plasma. As the latter defines the analytical outcome, accurate knowledge of the ion energy is very important. Therefore, the ions are also described with a MC approach in the CDS, together with the fast Ar atoms, which are created by charge transfer or elastic collisions of the ions [24].

These MC models for energetic electrons, and for ions and fast atoms in the CDS, together with the fluid model for slow electrons and ions, are solved iteratively, in which the output of one model is used as input for the next model, until convergence is reached [25].

Such MC and fluid models have also been developed for plasmas outside the analytical chemistry field, as they are relevant, e.g., in materials technology and for the semiconductor industry, for sputtering (e.g., [26–42]). While the conditions might be somewhat different, the methodology is very similar, and when developing the models for the analytical GDs, we based ourselves on these other models.

However, in analytical spectrochemistry, we are not only interested in the behavior of the electrons, Ar^+ ions, and fast Ar atoms, but we want to know how the sputtered atoms behave in the plasma, and how they get ionized and excited. Therefore, we extended the above hybrid MC–fluid model with other modules [43–48]. A schematic overview of the entire hybrid modeling network is presented in Fig. 1. It was developed for copper (Cu) as sample material, but the same approach can be taken for other elements, if the corresponding data is available.

When the Cu atoms are sputtered, they have a typical energy of 5–10 eV, which they quickly lose in the plasma upon collision with Ar atoms. This “thermalization” process is also described with a MC approach [43], and it yields a

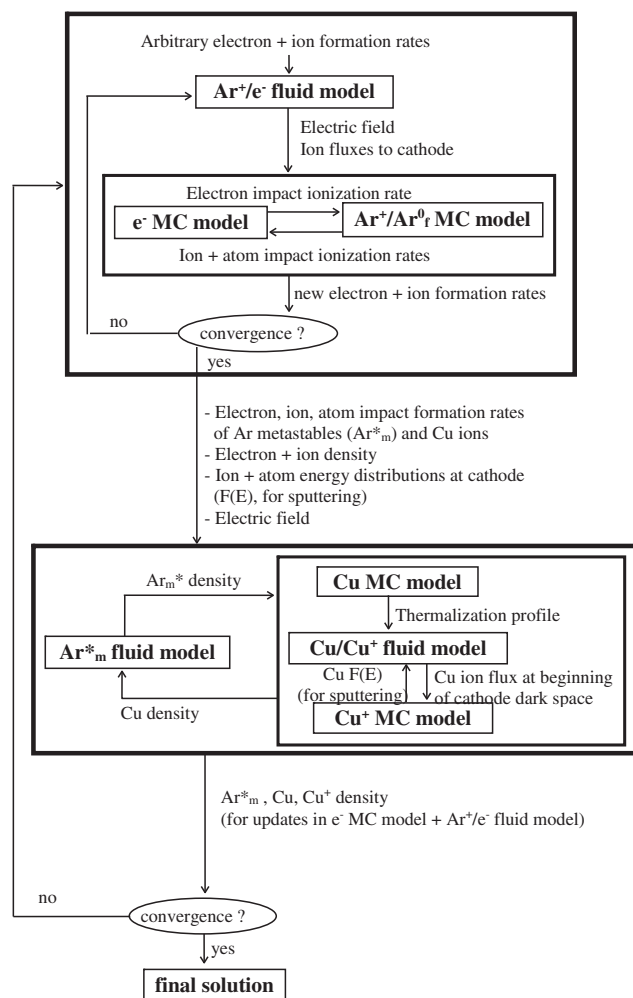


Fig. 1 Flowchart of the hybrid modeling network for a glow discharge plasma with (Cu) cathode sputtering

thermalization profile, which is used as input for describing the further behavior of the Cu atoms, including transport of the (thermal) Cu atoms by diffusion, as well as ionization and excitation, and the behavior of the corresponding ions and excited atoms and ions [44]. Ionization of the Cu atoms (and other elements) typically occurs by electron impact ionization, Penning ionization upon collision with Ar metastable atoms (Ar^*_m), and asymmetric charge transfer with Ar^+ ions.

The electron impact ionization rate is calculated in the electron MC model, while the rate of asymmetric charge transfer is obtained from the Ar^+ ion density, calculated in the electron– Ar^+ ion fluid model. To describe the Penning ionization, we need to know the Ar metastable atom density. Therefore, we developed a model specifically for the behavior of the Ar metastable atoms [45].

In addition, we also developed a detailed collisional–radiative model for the Ar atoms in 64 excited levels, including the metastable levels [47]. The behavior of all these excited levels is defined by collisions and by radiative decay, as dictated by the name of this model. This model also allows the

calculation of the optical emission spectrum of Ar, from the populations of all the excited levels. The latter is relevant for analytical spectrochemistry, to identify certain emission lines, but it is also of interest for optical plasma diagnostics of technological plasmas, as the line intensities (and line width) can give information on important plasma characteristics, like electron temperature and density, and the importance of certain processes and species. Hence, our collisional–radiative model for Ar was developed based on an existing model developed before for technological plasmas [49].

Likewise, we developed a collisional–radiative model for the Cu atoms in various excited levels, and the corresponding Cu^+ ions (in the ground state and various excited levels), as well as Cu^{2+} ions [48], which was based on a similar model developed for other applications, more especially for Cu^+ ion lasers [50]. This Cu collisional–radiative model also allows to calculate the optical emission lines of Cu, of interest for GD-OES, and in addition, the model provides information on the most important ionization mechanisms of Cu, by either electron impact ionization, Penning ionization, or asymmetric charge transfer, of interest for GDMS.

Finally, as the Cu^+ ions are also accelerated by the electric field in the CDS, and can give rise to cathode sputtering as well, their behavior in the CDS is also described with a MC model [44]. Again, all these models are coupled and solved iteratively [46], together with the electron– Ar^+ ion MC–fluid model above, until final convergence is reached; see details in Fig. 1 [51].

The above hybrid modeling network was initially developed for a direct current GD (see [51, 52] and references above), and the results were validated by several experiments. More specifically, in collaboration with researchers from the University of Florida, we applied laser-induced fluorescence and atomic absorption spectrometry to measure the absolute 2D density profiles of the sputtered atoms and ions [53] and of the Ar metastable atoms [54]. We also compared calculated sputter crater profiles with measured ones, for different GD sources, i.e., the VG9000 ion source used for GDMS [55] and the Grimm-type source typically used for GD-OES [56]. In addition, we compared calculated and measured optical emission intensities for Ar and Cu lines, both by end-on observation [57, 58], as well as by side-on observation, as a function of distance from the cathode, for which excellent agreement was reached, and important information could be obtained on the underlying processes [59, 60]. Together with researchers from IFW-Dresden, we measured electrical characteristics, sputter-erosion rates, as well as optical emission intensities of various Ar and Cu lines, for a range of conditions [61]. Finally, we collaborated with researchers from Indiana University for laser scattering experiments, to obtain information on the gas temperature (from Rayleigh scattering) and the electron number density, electron temperature, and shape of the electron energy distribution function (from Thomson

scattering), and we compared the spatial profiles with our modeling for a range of conditions [62, 63]. In general, good agreement was reached between our modeling results and all these experiments, giving confidence about the validity of our models.

Later, we extended the models to radio-frequency (RF) [64–69] and pulsed GDs [70–73]. In addition, we also described gas heating [74], gas flow [75], and cathode heating [76] with separate modules, added to the hybrid modeling network of Fig. 1. This is indeed a big added value of a hybrid model, i.e., several extra modules can be added to the modeling network. Finally, we also investigated the effects of adding H_2 [77–80], N_2 [81], or O_2 [82] to the Ar plasma. More information about all these models can be found in the cited references.

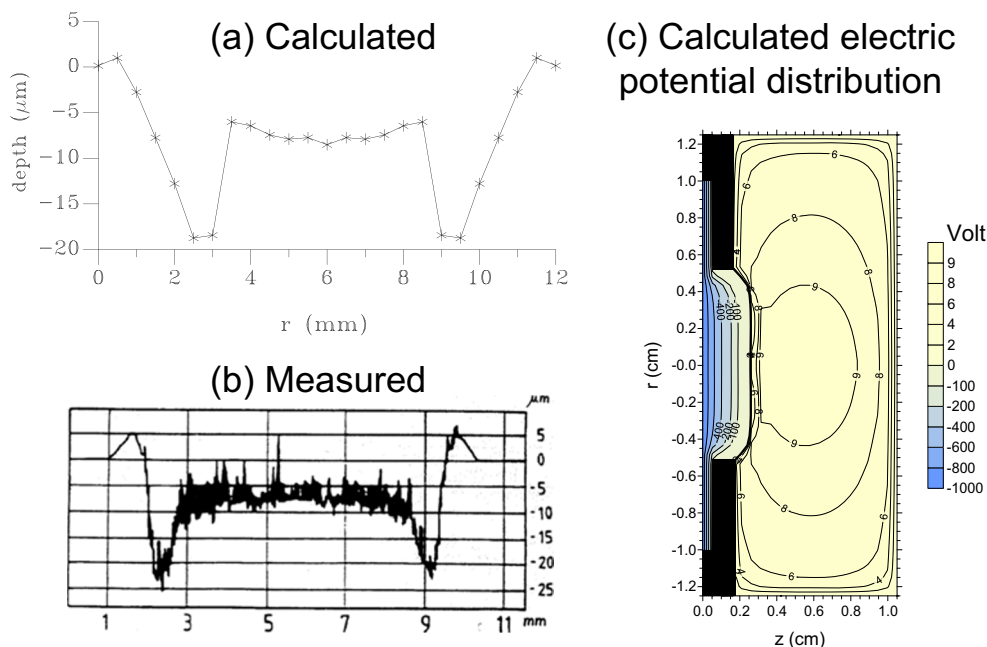
Characteristic results

The above modeling network gives information on the densities, fluxes, and energies (or energy distributions) of the various plasma species, as well as on the electric field and potential distribution, and the importance of various collision processes in the plasma. These results can be found in the references listed above. Here, we focus on some results of special interest for analytical chemistry.

Figure 2 a and b illustrate a calculated crater profile due to sputtering at the cathode, in comparison with a measured profile, for the VG9000 GD ion source [55]. We see that the crater is much deeper at the sides than in the center, both in the modeling results and the experiments. This so-called “crater edge effect” is not beneficial for depth profiling, because material from different depths will be sampled at the same time, drastically lowering the depth resolution. As the model can more or less reproduce the typical experimental crater profiles, it can be used to elucidate the underlying mechanisms. Indeed, when looking at the calculated electric potential distribution, plotted in Fig. 2c, it is clear that the equipotential lines are parallel to the cathode surface in the center, but they are bent near the sides, due to the presence of the cathode front plate, which is at anode potential and lies so close to the cathode that the equipotential lines are more concentrated in this region. The latter causes the Ar^+ ions to be focused more towards the edges of the cathode, explaining the typical shape of the crater profiles in Fig. 2a, b. Hence, based on the model predictions, it should be possible to develop improved GD source designs to avoid this effect.

The fact that other source designs are less prone to this “crater edge effect” is illustrated in Fig. 3a, b, presenting calculated and measured crater profiles for the Grimm-type GD, which is more commonly used for depth profiling analysis [56]. The crater profiles are now much more flat, and this can be explained from the calculated electric potential distribution, depicted in Fig. 3c, where the equipotential lines are

Fig. 2 Calculated (a) and measured (b) crater profiles due to cathode sputtering, in a VG9000 GD ion source, operating in Ar with Cu cathode, after 45 min of sputtering, at 75 Pa, 3 mA and 1000 V, as well as calculated electric potential distribution in this plasma at the same conditions (c), which can explain the “crater edge effect”, i.e., crater profile deeper at the sides than in the center, due to the curvature of the equipotential lines, focusing the ions towards the edges of the cathode



now more or less parallel to the cathode surface over the entire surface area, so that the Ar^+ ions are not focused anymore towards the edges, leading to much flatter crater profiles.

As explained in previous section, the hybrid modeling network developed for the GD also allows the calculation of optical emission line intensities, from the densities of the atoms in excited levels, obtained in the collisional–radiative model. Figure 4 a illustrates a calculated spectrum of Ar [57], while a spectrum of Cu is plotted in Fig. 4b, c [58]. Such spectra could be used to identify some lines in measured spectra and could thus in principle be helpful for supporting quantitative analysis.

While the spectra plotted in Fig. 4 are obtained by integration over the entire GD source, to mimic end-on observation,

the model also provides information on the emission intensities as a function of distance from the cathode. This is illustrated in Fig. 5a, for two Ar(I) lines, one Ar(II) line, and two Cu(I) lines, in a range of different conditions, and the same line emission intensities, obtained from experiments at exactly the same conditions, are plotted in Fig. 5b [59]. In general, quite good agreement is obtained, so the model can be used to explain the observed experimental profiles. For instance, the reason that the two Ar(I) lines exhibit a different profile is explained by the fact that the Ar(I) line at 750.38 nm originates from a lower Ar excited level than the Ar(I) line at 811.5 nm. The former is mainly populated by electron impact excitation, being most important in the beginning of the negative glow region (around 5 mm from the cathode; cf. Fig. 5a),

Fig. 3 Calculated (a) and measured (b) crater profiles due to cathode sputtering, in a Grimm-type GD source, operating in Ar with Cu cathode, after 157 s of sputtering, at 5 mA and 880 V, as well as calculated electric potential distribution in this plasma at the same conditions (c), showing more or less parallel equipotential lines, explaining why the crater profile is more flat than in Fig. 2

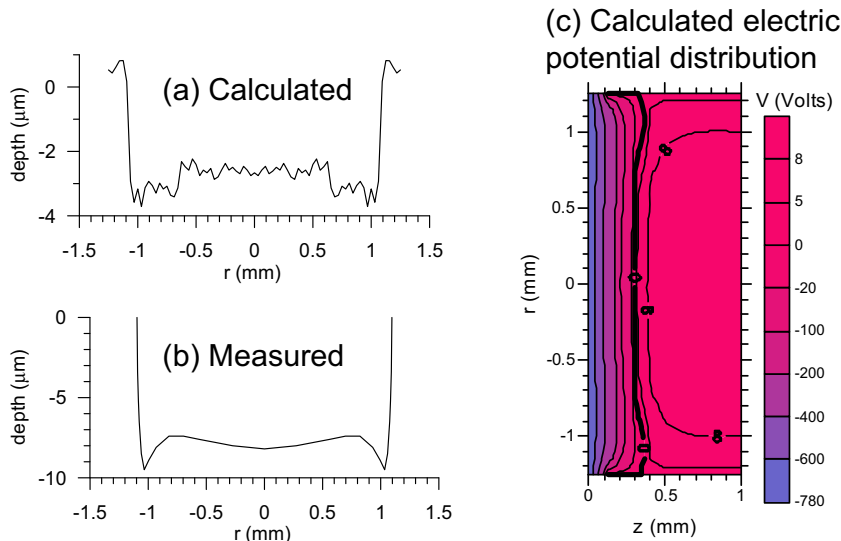
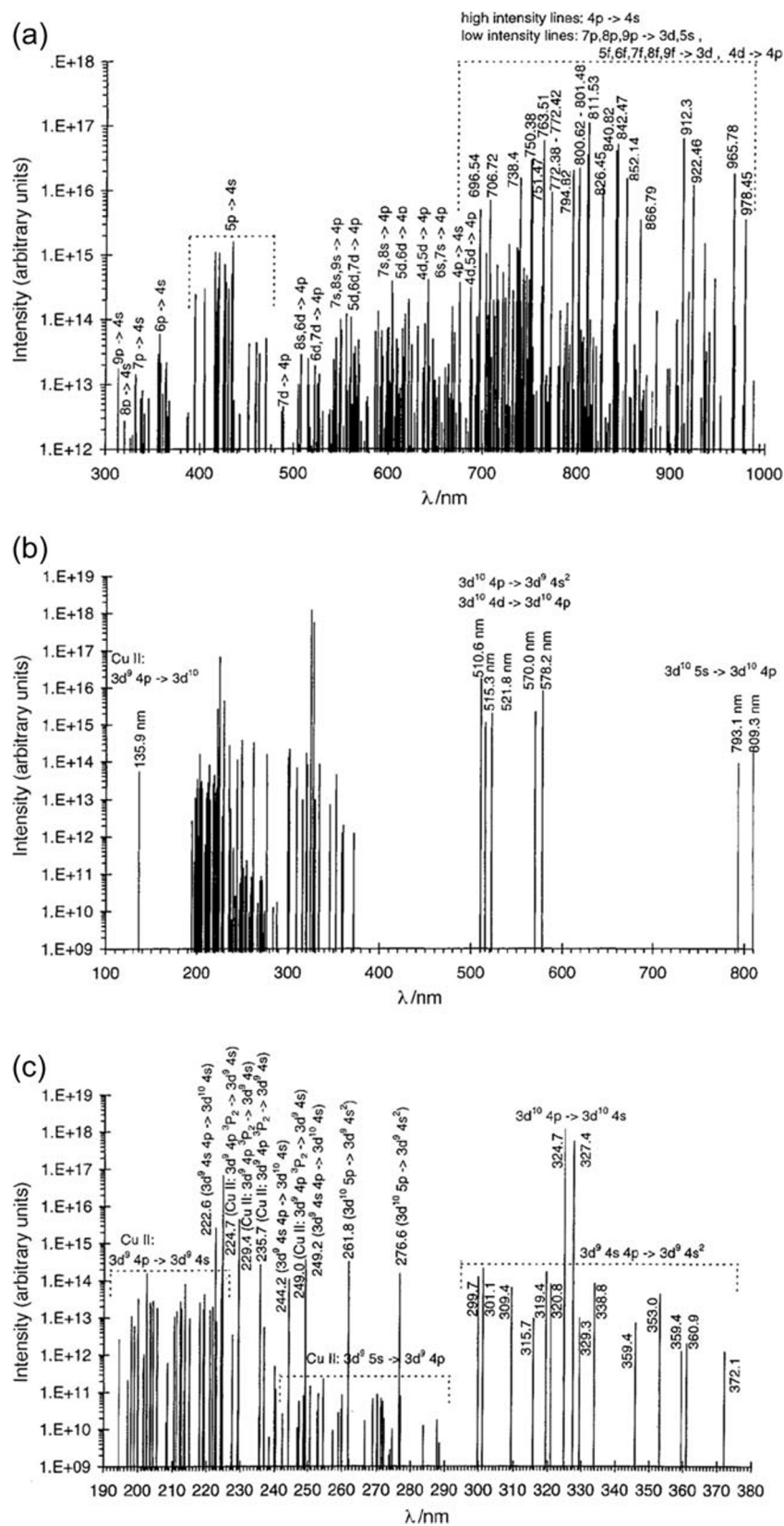


Fig. 4 Calculated spectrum of the Ar atoms lines (a), Cu atom and Cu⁺ ion lines (b), and detail of the Cu atom and Cu⁺ ion lines in a narrower wavelength range (c), in a Grimm-type GD source, by end-on observation, at 800 V, 500 Pa, and 28 mA. Adopted from [58] with permission



while the lower levels are also populated by excitation due to energetic Ar⁺ ions and Ar atoms, which only occurs close to

the cathode. This example illustrates how the modeling can provide insights into the underlying processes, which can be

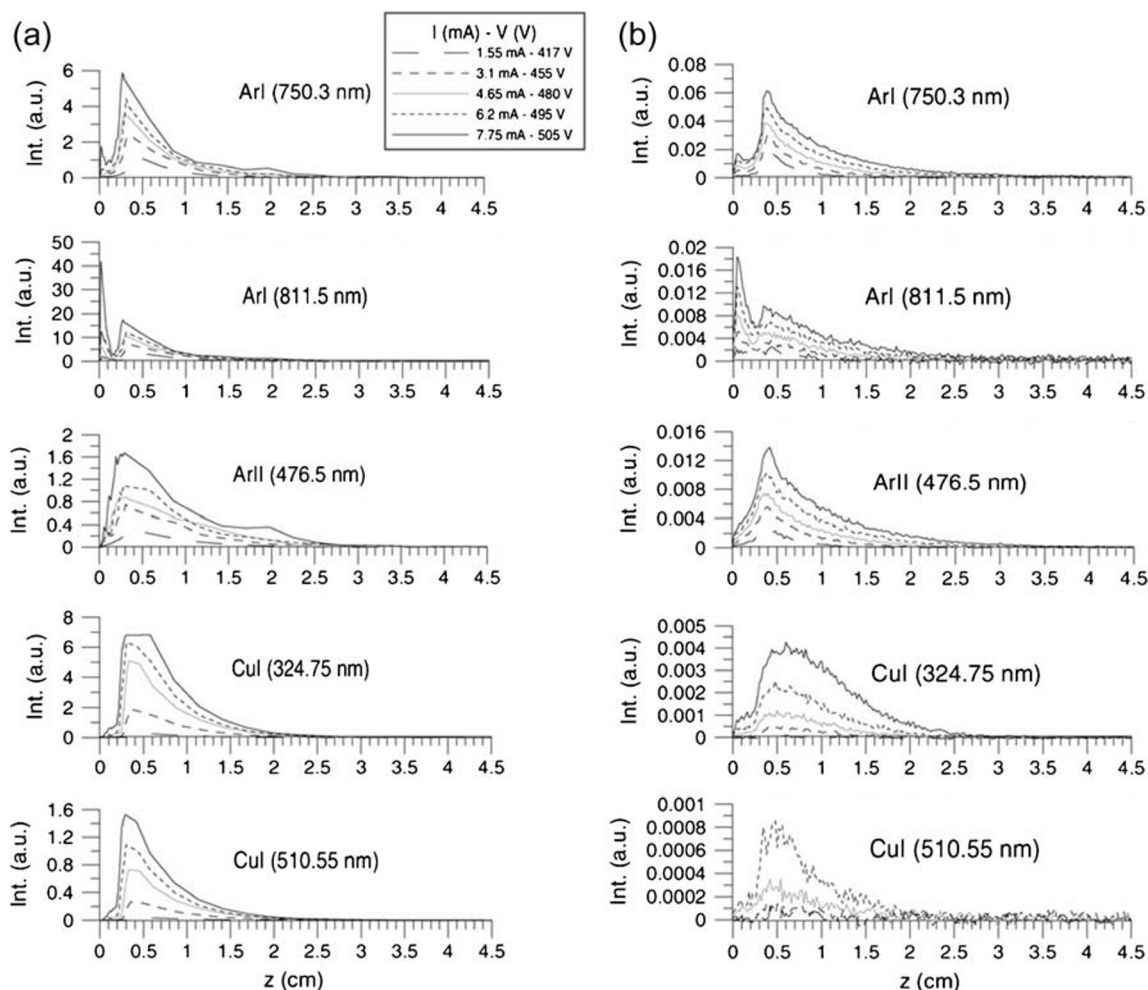


Fig. 5 Comparison of calculated (a) and measured (b) optical emission intensities, as a function of distance from the cathode, in a dc cylindrically symmetrical GD source, at a pressure of 80 Pa and five different currents

and voltages, as mentioned in the legend, for the lines Ar I (750.3 nm), Ar I (811.5 nm), Ar II (476.4 nm), Cu I (324.75 nm), and Cu I (510.55 nm). Adopted from [60] with permission

helpful for further improving the analytical performance of the GD source.

Finally, the insights obtained from these models allow us to gain information on the role of various ionization mechanisms of sputtered atoms, i.e., electron impact ionization, Penning ionization, and asymmetric charge transfer, and to link this information to variations in relative sensitivity factors (RSFs) used for quantification in GDMS [83]. Indeed, we found that the variations in these RSFs cannot all be explained by differences in the rates of electron impact and Penning ionization, but that asymmetric charge transfer is the main determining factor for these differences, as the efficiency of the latter process depends on the availability of excited ion levels lying close to the Ar^+ ion ground state or excited levels. Indeed, some elements possess such levels and can thus undergo asymmetric charge transfer, while other elements cannot, which is reflected in differences in their RSFs [83, 84].

Modeling of inductively coupled plasmas

Modeling approaches

In contrast to GDs, inductively coupled plasmas (ICPs) used in analytical spectrometry are in (or very close to) local thermal equilibrium (LTE). This means that the electrons locally exhibit the same temperature as the other plasma species, and the plasma can be described with one (plasma) temperature, being in the order of 10,000 K. The LTE assumption clearly simplifies the plasma modeling efforts and is thus the preferred method of choice for modeling an ICP. The ionization is simply described by the Saha-Eggert equation, and the number densities of all species, i.e., atoms and (singly, and doubly charged) ions of Ar and of the sample material (Cu is again taken as an example), as well as the electrons, are obtained based on the calculated ionization degree, the assumptions of quasi-neutrality, and conservation of heavy species [85]. On

the other hand, the gas flow dynamics is now more important than in GDs, where the gas flow rates are typically lower and the gas is most often considered to be static (see “[Modeling approaches](#)” in “[Modeling of glow discharges](#)”).

We calculate the gas flow dynamics in the ICP assuming laminar flow conditions, by solving conservation equations for mass and momentum (i.e., Navier–Stokes equation) for all gas flows, based on source terms. The source term for the mass conservation equation is the mass added to the continuous phase (i.e., gas phase) from the discontinuous phase (i.e., due to evaporation of the liquid droplets; see below), while the source term in the momentum equation is the Lorentz force. In addition, as the flow involves heat transfer, we solve the energy conservation equation, using the electric power density (calculated by Ohm’s law) as source term, and the emitted radiation as loss term. Moreover, a transport-diffusion equation is solved for the local mass fraction of each species. Finally, the electromagnetic field is calculated by the Maxwell equations.

The sample introduction is described with a so-called “discrete phase model (DPM)” (as opposed to the gas-phase (plasma) description, which is solved with a “continuous phase model” (CPM)). Cu is taken as an example, and introduced as elemental particles. We calculate the transport properties of the particles based on the actual temperature of the Ar gas flow. Hence, they are carried with the transport properties of first solid (300–1357 K) and then liquid phase (> 1357 K), up to reaching the vaporization point. We calculate the trajectory of each particle by the Newton equation, based on the drag force, i.e., a variation of the Stokes drag law, including the so-called Cunningham correction factor, and also taking into account the effect of Brownian motion.

Next to particle transport, heating of the particles is calculated by a heat and mass balance equation, and particle evaporation is described by mass transfer from liquid to vapor phase. As soon as the sample material reaches the vapor phase, the individual atoms are described by the conservation equations of mass, momentum, and energy, and by the Saha–Eggert equation (yielding the ionization degree at the local plasma temperature, based on the LTE assumption), just like for the carrier gas. Finally, the number densities of the atoms and ions of the sample material, as well as the electron density, are calculated from the ionization degree and the (mass and charge) conservation equations, just like for Ar.

In practice, we developed this model within Fluent (ANSYS), to which we added several user-defined functions (UDFs), i.e. self-written codes [85]. To our knowledge, this was the first self-consistent model for an ICP used in analytical chemistry, that focuses on the gas flow dynamics and plasma formation, and calculates the transport parameters for arbitrary mixtures of atomic species, based on the data from the pure elements, so that it could be applied to typical gas mixtures used in analytical chemistry, including carrier gas

and sample material. This model was validated by experiments, and good agreement was obtained [86].

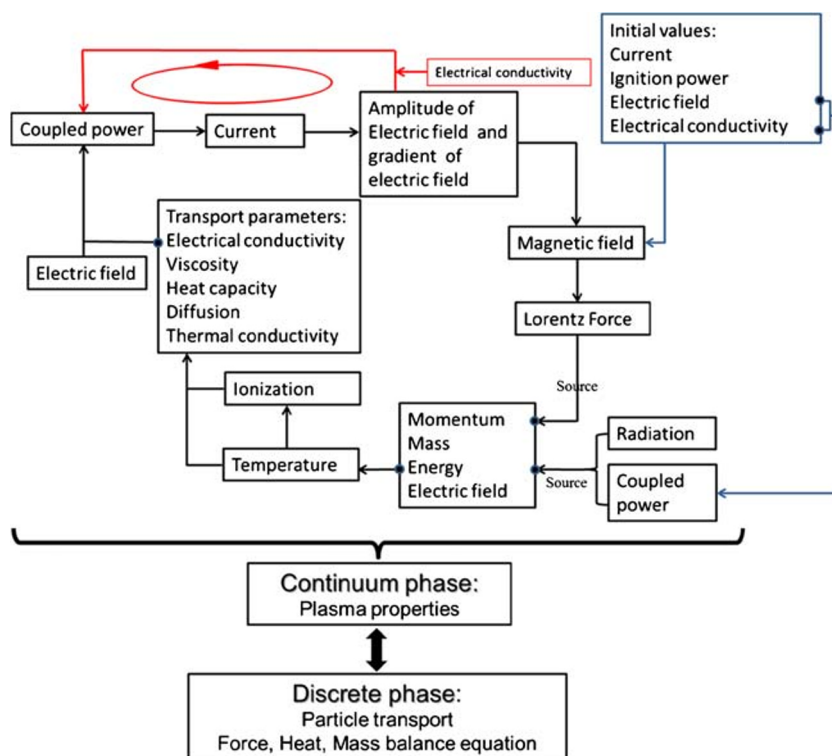
Subsequently, this model was extended to describe the ICP torch connected to a MS sampler cone, showing for the first time how the plasma characteristics are affected by a cool, grounded sampler, and by the sudden pressure drop behind this sampler [87]. We studied the plasma behavior for a range of different gas flow rates and applied power [88], and by varying the position and diameter of the sampling cone [89]. In addition, we studied the recirculation of the gas flow, in order to optimize the flow behavior inside the ICP [90].

Finally, we extended the model by incorporating the behavior of analyte material, i.e., elemental particles, using again Cu as an example. We followed the inserted particles throughout the ICP, up to the evaporation step [91], and we also included ionization of the particles [92]. From this model, we can trace the particles and determine their position and their phase (liquid, vapor, or ionized), velocity, and temperature, both in the ICP and at the sampler orifice. This allows us to determine the shape and position of the ion clouds, originating from either the Ar flow or the inserted sample material, which is of interest for both OES and MS studies.

The solution strategy of the model is depicted in Fig. 6 [93], and a detailed description can be found in the above-cited references. Note that this model describes the entire plasma region, from injector up to the sampling cone, but not the ion transport inside a MS.

This model was based not only on (and further developed from) models available in the literature, related to analytical spectrochemistry, but also from other fields, like for nanoparticle synthesis, where the ICP is typically created in much larger dimensions and often operates at much higher power (e.g., 5–25 kW) and lower frequency (e.g., 4 MHz). Most of the pioneering work on ICP modeling was performed by Mostaghimi, Proulx, and Boulos (see, e.g., [94–98], and see [93] for an overview of the evolution of their models). Although their models were not specifically developed for analytical spectrochemistry, in collaboration with Barnes [96] the authors developed a model for calculating the 2D emission pattern from a spectrochemical ICP as well. More recently, Colombo and coworkers performed outstanding modeling work for ICP torches, albeit mostly for higher power values and for other applications (e.g., nanoparticle synthesis) [98–101], but in collaboration with Mostaghimi, they also studied the behavior at a lower power of 300 W and a frequency of 40 MHz, of interest for spectroscopic analysis [101]. Likewise, Shigeta and coworkers also carried out a lot of computational work on ICP torches, focusing again on the production of nanoparticles, and for much larger ICP torches (e.g., a length of 180 mm and a diameter of 45 mm) and again much higher power and lower frequency [102–104]. Although the ICP in these other fields often operates at different conditions (i.e., higher power and lower frequency) and is

Fig. 6 Flowchart of the ICP model (for details, see text). Adopted from [93] with permission



created in much larger dimensions, the modeling approaches are quite similar, and insights obtained from these models can be very useful for modeling spectrochemical ICPs as well.

Characteristic results

Typical calculation results of the ICP model include the gas flow patterns through the ICP torch, the plasma temperature, and the electron density distributions, as well as information about sample transport, evaporation, and ionization. Some characteristic results will be presented here, at typical ICP conditions, i.e., 1 L/min injector gas flow rate, 0.4 L/min auxiliary gas flow rate, and 12 L/min outer gas flow rate, 1000 W plasma power, and 27 MHz frequency. The diameter of the injector inlet and sampler orifice are taken as 1.5 mm and 1 mm, respectively, and the sampling cone (with a temperature of 500 K) is positioned 10 mm from the load coil. As mentioned above, we considered Cu as the sample material, and the results presented here are for Cu particles of 1 μm diameter, injected at a mass loading flow rate of 100 ng/s.

The 2D profiles of the calculated plasma temperature and electron number density, as well as the gas flow velocity path lines, are plotted in Fig. 7. The temperature reaches a maximum of about 10,000 K near the coils. As a consequence, the electron number density also reaches its maximum (order of 10^{22} m^{-3}) in this region, caused by the higher ionization degree at higher temperature. Thus, the intense plasma is very localized, with a toroidal shape and a cool central channel.

The gas flow path lines are plotted in Fig. 7c. Note that the auxiliary gas path lines are drawn in black, to distinguish them from the injector gas and outer gas path lines, which are indicated in color. The injector gas exhibits typical velocities between 10 and 30 m/s, increasing at the sampling cone towards 100 m/s, and it moves more or less straight towards the sampling cone, with minimal expansion. Note that this flow pattern is typical for the conditions presented here, and can be different at other conditions (see details in [88]). The auxiliary gas has slightly lower velocities (order of 5–25 m/s) and shows backward motion (so-called recirculation), which is also affected by the discharge conditions (see [88, 90]). At the present conditions, all the auxiliary gas exits through the open ends of the ICP torch, and passes through the region of maximum power coupling (cf. purple contours in Fig. 7c), which is beneficial for efficient heat transfer, but again, this is not always the case, and depends on the conditions. Finally, the outer gas exhibits velocities of around 5–10 m/s.

The calculated 2D trajectories of the injected Cu particles, colored according to their temperature, are plotted in Fig. 8a. To indicate which gas path lines the Cu particles can follow, we added the gas path lines (of injector gas, auxiliary gas, and outer gas) to the figure as well, in black. The particles enter the ICP at room temperature in our model, but are gradually heated in the plasma until they reach the evaporation temperature (1850 K) and finally boiling temperature (2830 K). Once they are evaporated, they disappear as particles in the model, but they are further traced in the gas-phase domain.

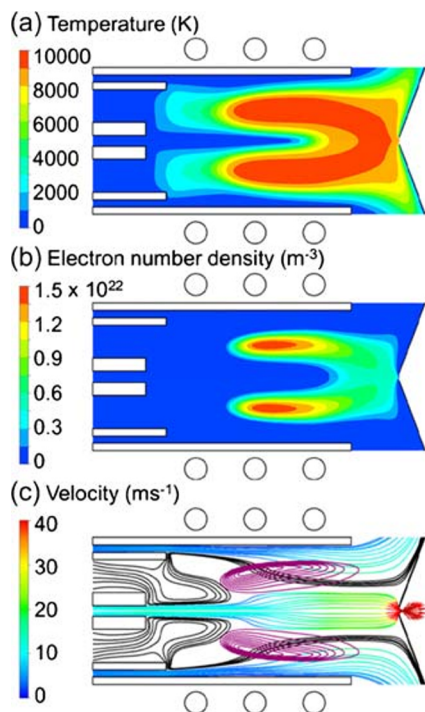


Fig. 7 2D profiles of the plasma temperature (a), electron density (b), and the gas flow velocity path lines (c), calculated for 1 L/min injector gas, 0.4 L/min auxiliary gas, and 12 L/min outer gas flow rate, a plasma power of 1000 W and 27 MHz frequency. The diameters of the injector inlet and sampler orifice are 1.5 and 1 mm, respectively. The sampling cone is placed 10 mm from the load coil. Note that the color scale in panel (c) indicates the gas velocity for the injector gas and outer gas, while the auxiliary gas flow path lines are colored in black, to distinguish them from the injector gas and outer gas. The purple contours in panel (c) indicate the region of maximum power coupling. Adopted from [93] with permission

The 2D evaporation rate of the Cu sample is presented in Fig. 8b. It is obvious that not all particles are evaporated at the same position in the plasma. Indeed, the particles follow the Ar gas flow path lines, which are subject to some radial expansion (cf. Fig. 7a). As a consequence, some gas path lines reach a higher temperature earlier in the torch (cf. Fig. 7a), and particles following these path lines will evaporate at earlier positions, while particles following the inner gas path lines stay longer at the cool central channel, and thus, they evaporate later in the torch.

As soon as the particles are evaporated, the Cu vapor atoms can become ionized, like the Ar gas. Figure 9 illustrates the 2D number density profiles of the Ar atoms, Ar^+ and Ar^{2+} ions, and of the Cu atoms, Cu^+ and Cu^{2+} ions. Note that the scales of the density profiles are different, to show more clearly the position of their maxima.

The Ar gas atoms are of course the most abundant. When entering the ICP, they have a number density of $2.4 \times 10^{25} m^{-3}$ (corresponding to atmospheric pressure and room temperature), but their density drops to around $6 \times 10^{23} m^{-3}$ inside the plasma, due to ionization, which mainly occurs in the coil

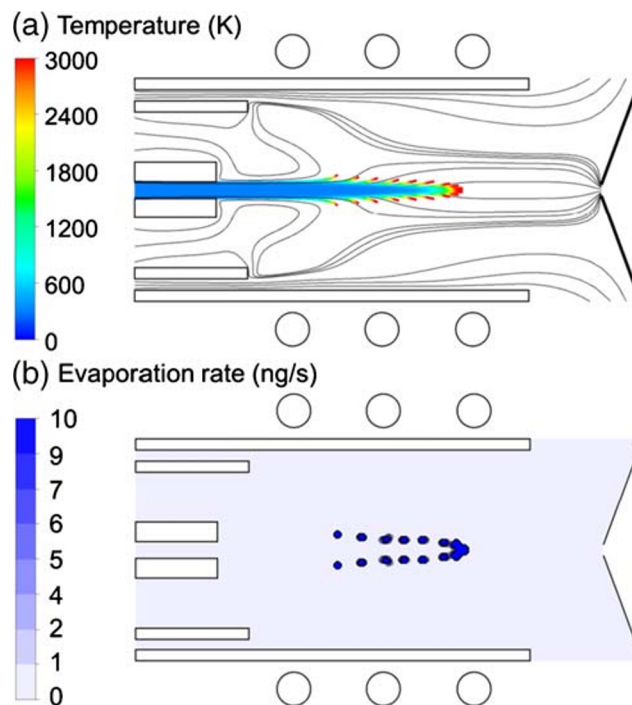


Fig. 8 2D trajectories of injected Cu particles, colored according to temperature, until they are evaporated, as well as the path lines of the injector gas, auxiliary gas, and outer gas, colored in black (a), and 2D distribution of the Cu evaporation rate (b), for Cu particles with diameter of 1 μm and mass loading flow rate of 100 ng/s injected from the injector gas inlet. The other conditions are the same as in Fig. 7. Adopted from [93] with permission

region, at the position of maximum temperature (cf. Fig. 7 above). As a result, the Ar^+ ion number density reaches a maximum (of $1.5 \times 10^{22} m^{-3}$) in this region. The same applies to the Ar^{2+} ion number density, but its maximum density is slightly below $10^{14} m^{-3}$, hence eight orders of magnitude lower. Thus, further ionization of the Ar^+ ions into Ar^{2+} ions is virtually negligible, due to the high second ionization potential of Ar (i.e., 27.7 eV). The ionization degree of Ar (calculated from the volume-integrated densities over the entire torch) is around 0.027%.

The Cu atoms are characterized by a maximum number density at the position of maximum evaporation (cf. Fig. 8b above). When integrated over the entire ICP torch, their density is more than seven orders of magnitude lower than the Ar gas atom density, at the mass loading flow rate studied here (100 ng/s). The Cu^+ ions reach their maximum density at the central axis, at the position of maximum evaporation and where the plasma temperature rises (cf. Fig. 7a above). The Cu^{2+} ions, however, reach their maximum density in the region of maximum temperature, like for Ar. It is important to mention that the Cu^+ and Cu^{2+} ion densities are still significant near the sampler, which is important for the application of ICP-MS. When integrating over the entire ICP, the overall ionization degree of Cu is around 60%, i.e., much higher than for Ar, due to the lower ionization potential of Cu (i.e.,

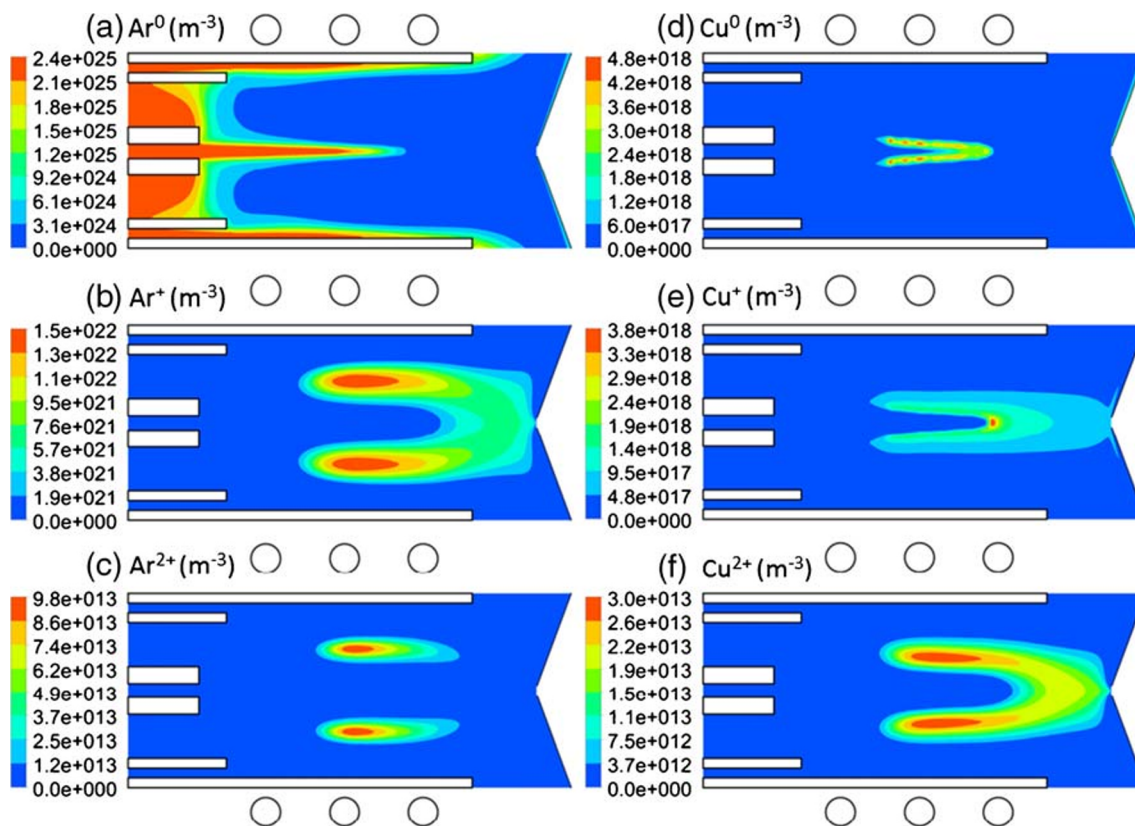


Fig. 9 2D number density profiles of the various species in the ICP: Ar^0 (a), Ar^+ (b), Ar^{2+} (c), Cu^0 (d), Cu^+ (e), and Cu^{2+} (f), for Cu particles with a diameter of 1 μm and mass loading flow rate of 100 ng/s injected from

the injector gas inlet. The other conditions are the same as in Fig. 7. Adopted from [93] with permission

7.73 eV vs 15.76 eV for Ar). However, only a small fraction (about 0.001%) of the Cu^+ ions is further ionized into Cu^{2+} ions. Nevertheless, this fraction is much higher than that for Ar, again due to the lower second ionization potential of Cu (i.e., 20.9 eV vs. 27.7 eV for Ar).

Finally, Fig. 9 indicates to what extent the different species expand in the torch, useful for the application of both ICP-OES and ICP-MS. For ICP-MS, the fluxes of the various species at the position of the sampler orifice is of most interest. The fraction of Cu^+ ions arriving at the sampler orifice with respect to the amount of Cu injected in the ICP (which is a measure of the Cu sample transport efficiency from injector gas inlet towards entering the MS) is calculated to be about 42% for the conditions presented here. However, it depends on the operating conditions, and especially on the injection position in the injector gas inlet (see details in [92]).

We applied this model to a wide range of operating conditions. More specifically, we studied the effect of the presence of a sampling cone [87], the influence of gas flow rates and plasma power [88], of sampler orifice diameter and position [89], of injector inlet diameter and position of particle injection [91], as well as of the particle diameter and particle loading flow rate [91, 92], and we found that these conditions largely affect the ICP characteristics and the behavior of the

sample material, as discussed in detail in our previous papers [87–93]. In summary, this model provides insight into how the operating conditions and geometry can be optimized to improve the analytical performance of ICP-MS.

Modeling of laser ablation for ICP and LIBS

Modeling approaches

Modeling of laser ablation (LA) and laser-induced plasma formation (like for LIBS) is also most often based on the LTE assumption, which is indeed the most straightforward approach, like for the ICP (cf previous section), and again, the difficulty in modeling is mainly attributed to the fluid dynamics of the vapor plume expansion and interaction with the background gas, which must again be described with Navier–Stokes equations.

We developed a model that accounts for laser–solid interaction, causing heating, melting, and evaporation of the target material, followed by vapor plume expansion, plasma formation, and laser–plasma interaction [105, 106].

The temperature distribution inside the target material, as a consequence of target heating, is calculated with a heat

conduction equation. When the temperature reaches the melting point, melting of the solid material will occur, but the same heat conduction equation can be used, albeit with material properties for the molten phase. At still higher temperature, vaporization can occur, so the vapor density, velocity, and temperature can be calculated, and they serve as boundary conditions for describing the vapor plume expansion.

Initially, we developed a model for vapor plume expansion in vacuum [105], but later we extended this model to expansion into 1 atm background gas, including the description of the interaction between vapor and gas [106], and we compared the behavior with expansion in vacuum [107]. The expansion of the vapor plume in background gas is described with Navier–Stokes equations, for conservation of total mass density, vapor mass density, momentum, and energy in a binary gas mixture.

As a consequence of the high temperature in the plume, both the vapor and background gas become ionized, creating a plasma. For the background gas, only singly charged ions are typically taken into account, because further ionization is negligible, but the target material generally has a lower ionization potential than the background gas (see also “Modeling approaches” in “Modeling of inductively coupled plasmas”), so that also doubly charged ions are considered. As mentioned above, the plasma can be considered in LTE, so the first-order (and second) ionization degrees of metal and gas are calculated from the plume temperature, with Saha-Eggert equations, like in the ICP model.

Finally, the laser beam will also interact with the created plasma, and it will partially be absorbed before reaching the target (so-called plasma shielding). The model accounts for several absorption mechanisms, i.e., electron-neutral and electron-ion inverse Bremsstrahlung, as well as photoionization from excited levels (see [105] for more explanation).

The various parts of the model are strongly coupled, because the sample evaporation affects the vapor plume expansion dynamics, while the vapor defines the boundary conditions for the target material. In addition, absorption of the laser beam inside the plasma reduces the effective laser irradiance that can reach the target, and it gives rise to heating of the plasma. Therefore, the different parts of the model must be solved simultaneously as a function of time. This creates an integrated picture of LA, plume expansion and plasma formation. For details of the model, i.e., equations and solution procedure, boundary conditions, and coupling of the various parts, we refer to [105, 106].

Finally, besides modeling the process of laser ablation (LA), vapor plume expansion, and plasma formation, we also developed models for describing LA cells, in order to better understand the gas flow patterns and to improve LA chamber designs for optimal sample introduction in the ICP (see examples in next section). This modeling is again based on fluid

dynamics simulations, which is the most suitable approach for this purpose, certainly at atmospheric pressure. Indeed, another approach would be direct MC simulations, but the latter only have added value (higher accuracy) at low pressure, while at atmospheric pressure this approach would require much longer calculation times. More details of the simulation setups can be found in [108–112].

Characteristic results

The models for LA, plume expansion, and plasma formation provide information on the target temperature, melt and evaporation depth, the density, velocity, and temperature profiles in the vapor plume (and the background gas), and the ionization degree in the plasma. These results will be illustrated for LA of a Cu sample, expanding in 1 atm He background gas. We assume a Gaussian-shaped laser pulse with 10 ns full-width at half-maximum (FWHM) and peak laser irradiance of 4×10^8 W/cm². Integrated over the entire laser pulse, this gives a fluence of 4.24 J/cm². The laser wavelength is taken as 266 nm, and the target reflectivity is assumed to be 0.34. In the calculations, we follow only one laser pulse.

The calculated temperature distribution in the target upon laser–solid interaction, as a function of time during and after the laser pulse, is plotted in Fig. 10. Initially, the target temperature is assumed to be 300 K, but it rises rapidly to ca. 7000 K at about 20 ns, after which it drops again. However, the temperature drop is much slower than the temperature rise, so that after 100 ns the temperature at the surface is still about 1500 K. As expected, the temperature reaches its maximum at the target surface, but due to heat conduction, the temperature inside the target is also elevated up to about 10 mm distance.

Figure 11 illustrates the calculated melt and evaporation depth as a function of time during and after the laser pulse. Melting occurs as soon as the target temperature rises above

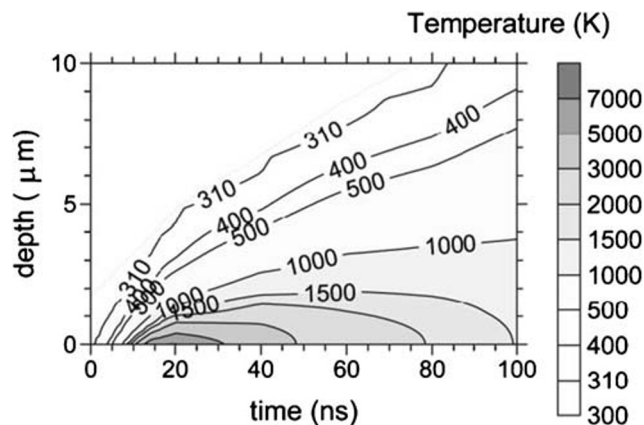


Fig. 10 Calculated temperature distribution in the Cu target, as a function of time during and after the laser pulse, for LA of a Cu sample, expanding in 1 atm He background gas, assuming a Gaussian-shaped laser pulse of 266 nm, with 10 ns FWHM and peak laser irradiance of 4×10^8 W/cm², yielding a fluence of 4.24 J/cm². Adopted from [107] with permission

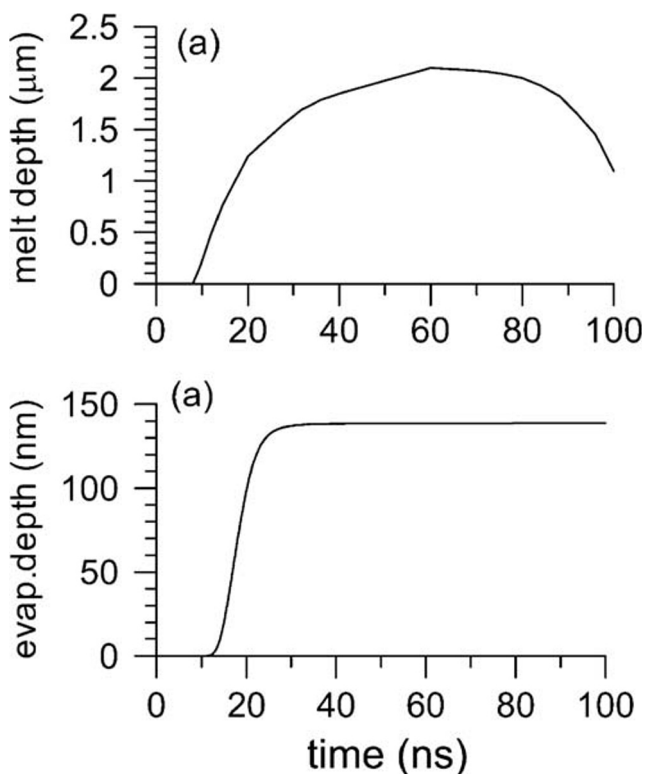


Fig. 11 Calculated melt depth (a) and evaporation depth (b) in the Cu target, as a function of time during and after the laser pulse, for the same conditions as in Fig. 10. Adopted from [107] with permission

1358 K (melting point of Cu), i.e., at about 10 ns. The melt depth is at maximum ca. 2 mm at 60 ns, after which the target cools down slowly, so that the melt depth (or depth of molten material) drops again, to about 1 mm at 100 ns (see Fig. 11a).

The evaporation depth (Fig. 11b) starts rising after ca. 12 ns, till it reaches a value of ca. 140 nm after 25–30 ns. Indeed, most evaporation occurs between 12 and 25 ns, during the laser pulse. Subsequently, the evaporation stops, and thus the evaporation depth remains constant.

It is interesting to mention that this model only considers material removal by evaporation, while in reality, splashing of molten material due to the recoil pressure of the plume can take place as well, also contributing to material removal. The latter mechanism can be quite important, because measured crater depths after one laser pulse are reported to be in the order of a few μm, hence comparable with the melt depth in Fig. 11, indicating indeed that molten material will largely be ejected by this mechanism [113].

The calculated 1D density profiles (as a function of distance from the target) of the evaporated Cu material and the He background gas are plotted in Fig. 12, at various times. At 20 ns, the Cu density reaches its maximum near the target due to evaporation. Subsequently, once the evaporation process has stopped (cf. Fig. 11), the Cu density yields a broader profile with a lower maximum and further away from the target, because the Cu atoms are spread out due to expansion.

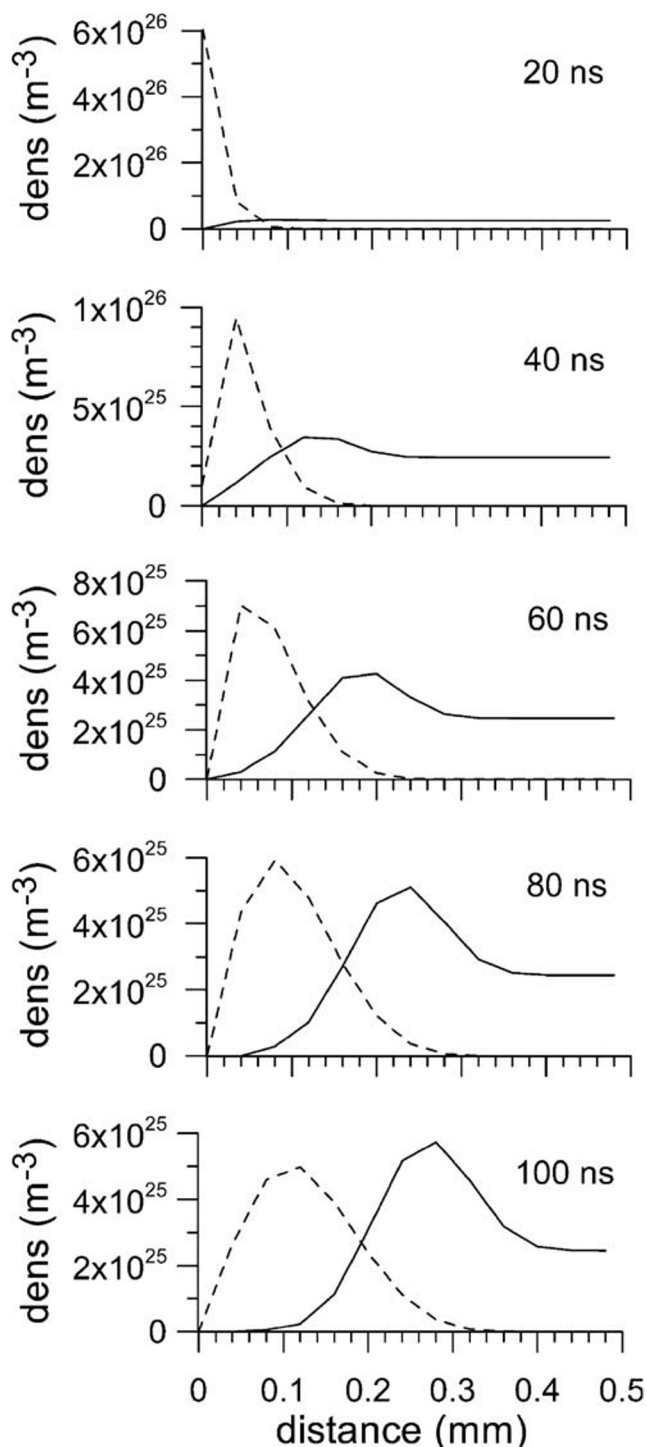


Fig. 12 Calculated density profiles of the evaporated Cu plume (dashed lines) and the He background gas (solid lines), at different times, for the same conditions as in Fig. 10. Adopted from [107] with permission

The vapor plume expansion also causes the He background gas to be pushed away from the target, yielding a peak just in front of the vapor plume.

The evaporated plume velocity and plume temperature at different times are plotted in Fig. 13 as a function of position from the target. The plume velocity reaches values of about

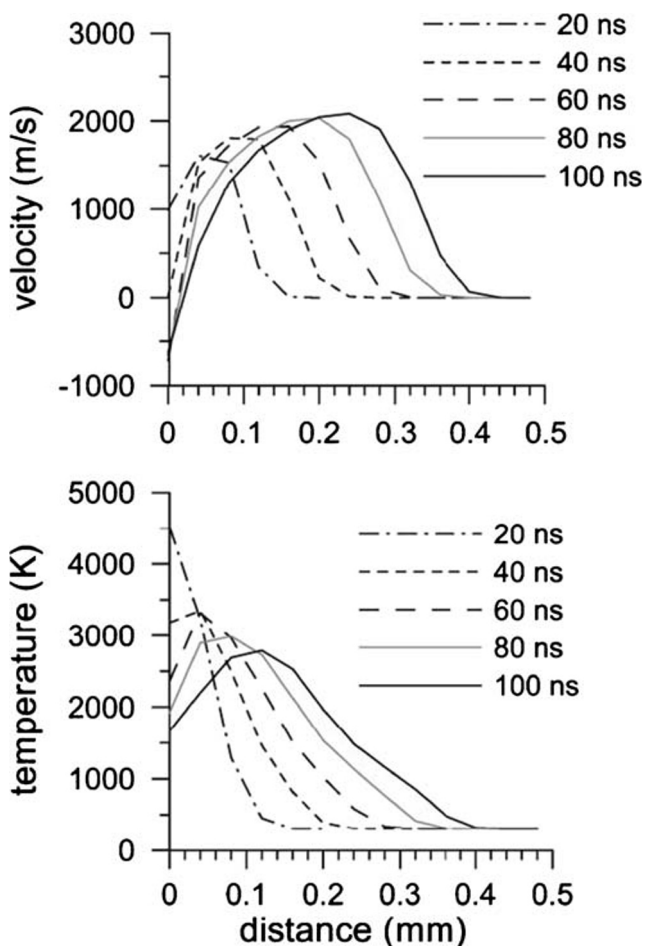


Fig. 13 Calculated plume expansion velocities (top) and temperature distributions in the plume (bottom), at different times, for the same conditions as in Fig. 10. Adopted from [107] with permission

1000–2000 m/s. Once evaporation is finished, part of the plume still moves away from the target, while the other part moves towards the target, due to the background gas pressure. This so-called recoil of the plume gives rise to splashing of the molten material, as mentioned above. The plume temperature reaches its maximum (of about 4500 K) near the target at 20 ns, but at later times, the maximum shifts away from the target and drops to lower values, although it is still above 2500 K after 100 ns.

These results apply to a Cu sample, expanding in 1 atm He background gas, for one laser pulse with fixed duration (10 ns FWHM), irradiance (4×10^8 W/cm²) and wavelength (266 nm), but we also studied the effect of the laser parameters on the LA process and the laser-induced plasma formation [114], as well as the effect of expansion in different background gases [115] and different pressures of the background gas [116]. Moreover, we also compared the behavior of various metals (Cu, Zn, Al, Fe, Mn, and Mo), by modeling and experiments [117]. We found that the material properties, more specifically the target surface reflectivity, optical absorption coefficient, thermal diffusivity, and melting/boiling

temperature, largely influence the target surface temperature and the amount of laser-induced vaporization, and thus they also affect the plume expansion, plasma formation, and plasma shielding.

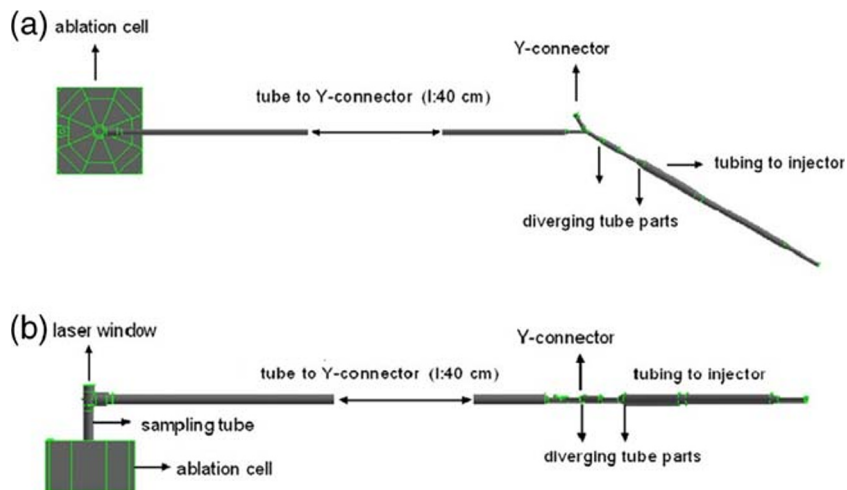
We also studied the behavior of double pulse (DP) LA and LIBS [118]. We varied the interpulse times between 10 and 100 ns and compared the results with those of a single pulse (SP) with the same total energy. The maximum surface temperature was a bit lower in the DP configuration, because of the lower irradiance of one laser pulse, but it remained high for a longer time, because it could rise again upon the second laser pulse. As a result, the target remained in a molten state for a longer time, suggesting that DP-LA might be more efficient, through the mechanism of splashing of the molten target (cf. above). In addition, the total laser absorption in the plasma was clearly lower in the DP configuration, so that more laser energy could reach the target and contribute to LA. Finally, the plume expansion dynamics was characterized by two separate waves, originating from the first and second laser pulse. After 200 ns, the plasma temperature and electron density were slightly higher than in the SP case, especially for longer interpulse times.

Finally, as explained in section 4.1, we also developed fluid dynamics simulations for describing LA cells [108–112]. These simulations showed how the flow characteristics of the carrier gas affect the sample introduction and signal intensities. In addition, we modeled transient signals for repeated laser shot analysis, calculating the convolution of a single shot profile with the laser pulse sequence profile [108].

We also studied the performance of several sample chambers [109] and demonstrated that the geometry and size can greatly affect the gas velocity pattern and the extraction efficiency. While the extraction efficiency of conventional ‘drum-shaped’ cells (with a volume between 3 and 100 cm³) was between 5 and 15% (number of particles), the calculations revealed a factor six enhancement in extraction efficiency for optimized designs. In addition, helium and argon were compared as carrier gases. The calculations predict that He improves the transport speed and extraction reproducibility of large volume cells, while Ar showed better extraction efficiency especially for finer particles, due to a shorter mean free path, which mitigated nanoparticle slipping [109].

As an example, Fig. 14 schematically illustrates a LA setup, in top and side view, including ablation cell (outer chamber), sampling tube, and transport tubing towards the ICP injector, for which we performed fluid dynamics simulations. Figure 15 presents the calculated gas flow path lines in the LA cell and sampling tube. For the sake of clarity, only a few of the hundreds of calculated flow lines are plotted. The flow lines in the outer chamber reveal some vortices next to the flow inlet. The onset of the flow is turbulent, but the flow pattern in the sample tube is clearly laminar. Furthermore, a weak turbulent zone can be observed in the volume under the

Fig. 14 Top view (a) and side view (b) of a LA setup, including ablation cell, sampling tube, and tubing towards the injector for the ICP, described by computational fluid dynamics simulations. Adopted from [110] with permission



laser window (see detail in Fig. 15). However, in general, the laminar flow pattern is nicely conserved till it reaches the Y-connector (cf. Fig. 14).

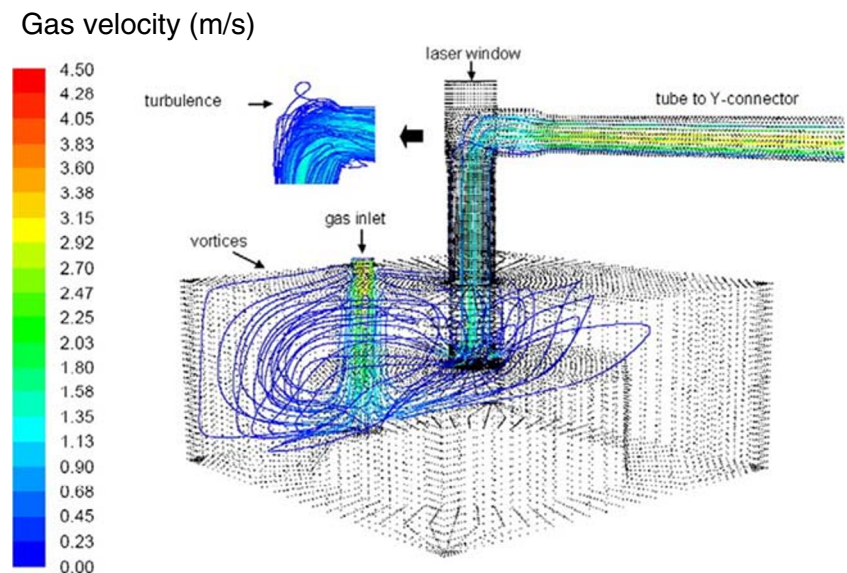
At the Y-connector, however, the situation dramatically changes (see Fig. 16). The flow of the auxiliary flow gas (Ar) pushes the carrier gases (He or Ar) that arrive from the sample chamber towards the wall. This causes surface friction, resulting in small eddies in the wall region opposite to the Ar gas inlet (Fig. 16a). At the diverging parts of the tubing, where the Y-connector and injector are connected, the flow pattern is clearly turbulent.

Our model also allowed to calculate the transient signal fine structure, based on mass transport efficiency and transit times of near-infrared femtosecond (fs) laser-generated brass aerosols, and predicted a bimodal peak structure, due to turbulent effects in the tubing connecting the Y-connector and injector (see Fig. 16), which was experimentally validated [110].

In [111] an optimized LA setup for high repetition rate ICP-MS analyses was described, e.g., for 2D imaging or depth profiling, where the particle washout time needs to be as short as possible to allow high laser pulse frequencies for reduced analysis time. The fluid dynamics simulations allowed us to modify an existing LA setup, so that it operated in the laminar flow regime, confirmed by experiments. Furthermore, we gave recommendations towards a modified setup for more resilient spatial distributions, reaching a washout time of 140 ms, so that 7 Hz repetition rates could be applied.

The same approach was adopted in [112], for studying a specific LA cell, i.e., the high-efficiency aerosol dispersion (HEAD) cell. We analyzed the particle transport, as well as the critical velocity for the onset of particle losses, and we calculated the transport efficiency through the Venturi chamber for different sample gas flow rates. Our calculations predicted that small particles were mainly lost at low flow rates, while large particles were predominantly lost at higher flow

Fig. 15 Calculated gas flow path lines in terms of velocity (m/s), in the LA cell and sampling tube, depicted in Fig. 14, for a He/Ar mixture. The flow rate in the LA cell was 0.79 L/min (for Ar) and 1.3 L/min (for He). The pressure and temperature were 1 atm and 300 K. For the sake of clarity, 80% of the carrier gas path lines are omitted. At the inlet of the LA chamber, a rotational flow structure can be observed, but in the sampling tube and transport tube, the flow is clearly laminar, except in the zone under the laser window (see detailed flow pattern nearby the laser window in the inset). Adopted from [110] with permission



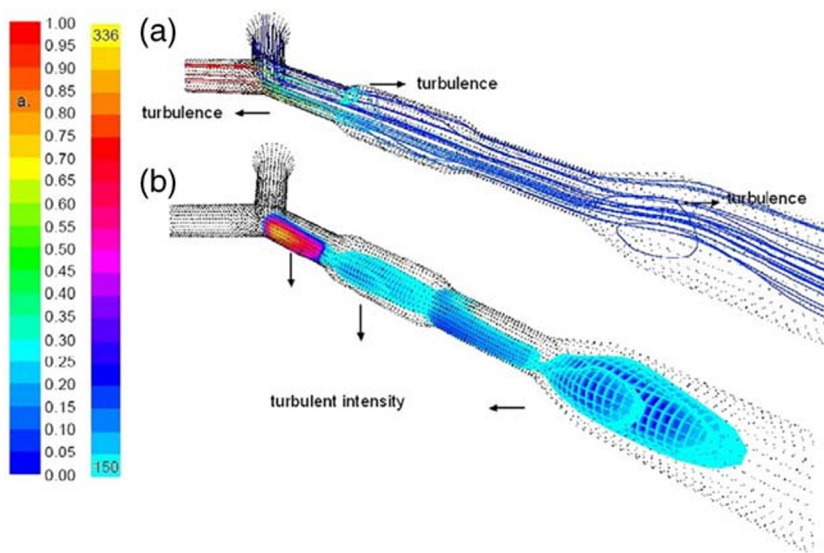


Fig. 16 **a** Calculated gas flow pattern in the tubing connecting the Y-connector and injector, for the LA cell and sampling tube depicted in Fig. 14, in terms of the mass fraction of He (red is 100% He, blue lines correspond to 0% He or 100% Ar). The flow rate in the LA cell was 0.79 L/min (for Ar) and 1.3 L/min (for He), while the flow rate in the

Y-connector was 1.55 L/min (Ar). The pressure and temperature were 1 atm and 300 K. For sake of clarity, only a part of the gas path lines are plotted. Three turbulent regions are indicated. At the diverging tube parts, the eddies can clearly be observed. **b** Zones of maximum turbulent intensity (%) (see details in [110]). Adopted from [110] with permission

rates. In addition, we proposed a modified HEAD cell, based on the simulation results, which resulted in extremely short calculated washout times. As this LA cell consists of different modular parts, the results are also of potential interest for other LA cells.

Modeling of other plasma sources used in analytical chemistry: Insights by cross-fertilization from other fields

In recent years, there is growing interest in atmospheric pressure non-thermal plasmas (NTPs) for analytical chemistry, such as dielectric barrier discharges (DBDs), atmospheric pressure glow discharges (APGDs), and various plasma sources for ambient desorption/ionization coupled with MS [15]. These plasma sources produce energetic species that react with ambient air components to generate reagent ions (such as protonated water molecules and clusters, N_2^+ and O_2^+), which can ionize both polar and non-polar species for analysis by MS. In addition, the beam of excited and ionized He and the reagent ions is rather warm, or can be heated, and can thus directly desorb volatile species from a sample surface. Thus, the ambient source can be aimed at a sample in the open atmosphere and the desorbed and ionized species drawn into an atmospheric sampling inlet of an MS, resulting in a “clean” mass spectrum of species from the sample surface, without requiring any sample pre-treatment.

In spite of the powerful capabilities of these plasma sources for ambient mass spectrometry, more fundamental insight in the underlying mechanisms is crucial, to overcome the current

limitations, such as matrix effects, and irreproducibility because of inconsistencies in positioning of the source, sample, and inlet to the MS. This fundamental insight can be obtained by experiments, but again computer modeling can be very useful as well.

As these new sources operate at atmospheric pressure, characterized by high collision probabilities, fluid modeling is usually sufficient for an accurate description, as the energy gained by electrons and ions can be lost again by collisions (see detailed discussion on various modeling approaches, and their benefits and limitations, in “Modeling approaches” in “Modeling of glow discharges”). Hence, we developed a 1D fluid model for a DBD in He, used for analytical chemistry, e.g., as microchip plasma source [119]. The model provided information, among others, on the potential distribution inside the plasma, as well as the potential drop across the dielectrics, the electric current, and gap voltage as a function of time for a given applied potential profile, the spatial and temporal number density profiles of the different plasma species, and the importance of various production and loss processes for these species. In [120], we applied this model to investigate the effect of pressure on the plasma characteristics. We showed that the discharge current, as a measure for the plasma activity, was significantly higher for pressures ranging from 50 to 140 mbar, compared with atmospheric pressure.

When combining such a fluid model with MC simulations into a hybrid model (see again detailed discussion in “Modeling approaches” in “Modeling of glow discharges”), the non-equilibrium behavior of the electrons can more accurately be described, providing additional information on electron impact ionization and excitation rates. Therefore, we also

developed a combined fluid model and MC simulations for an APGD in He, also used for analytical spectrometry [121]. These models also provided information on the potential and electric field distributions, the density profiles of the various plasma species, the mean electron energy, as well as the importance of the different production and loss processes for the various species. Furthermore, we discussed the similarities and differences with low-pressure GDs. For instance, an APGD is characterized by a much smaller cathode dark space region and a large positive column, compared with low-pressure GDs, and molecular ions play a much more important role.

Figure 17 illustrates the calculated 2D number density profiles of the He^+ , He_2^+ , N_2^+ , and N_4^+ ions in the plasma, for an APGD developed by Hieftje and coworkers [122], operating at a He pressure of 1 atm with 10 ppm N_2 impurities, a DC voltage of 650 V, an electric current of 30 mA, and a gas temperature of 1350 K.

The He^+ density (Fig. 17a) reaches a pronounced maximum of $2.3 \times 10^{18} \text{ m}^{-3}$ near the cathode and a second maximum of about 10^{18} m^{-3} near the anode tip, but in between both peaks, the density is virtually zero. The He_2^+ density (Fig. 17b) also shows two maxima, in the same order of magnitude, but the second maximum is clearly higher (up to $2.5 \times 10^{18} \text{ m}^{-3}$) and broader. Moreover, the density is non-zero in between these maxima, reaching values around 10^{18} m^{-3} . Thus, overall, the

He_2^+ ions are present at a higher density than the He^+ ions, which is indeed common for APGDs.

The N_2^+ and N_4^+ ion densities do not exhibit a second maximum near the anode, but they gradually drop as a function of distance from the cathode (see Fig. 17c, d). The N_2^+ ion density is only slightly lower than the He^+ and He_2^+ densities, in spite of the fact that N_2 is only present as impurity, with density of five orders of magnitude lower than the He gas density. Thus, the ionization degree of N_2 is significantly higher than the He dissociation degree, i.e., in the order of 10^{-3} – 10^{-2} vs 10^{-7} . This finding is important for analytical chemistry, because it suggests that the APGD in He can efficiently ionize gaseous analytes or aerosols, for detection with MS [122]. Hieftje and coworkers also observed intense emission from the APGD, attributed to N_2^+ bands [122]. The N_4^+ ions, on the other hand, are characterized by a density that is two orders of magnitude lower than the other ion densities.

Farnsworth and coworkers also developed a model for a DC glow discharge in He, used as ambient desorption/ionization source for MS [123]. The model included both the fluid dynamics of the flowing gases as well as the chemical reaction kinetics. The calculation results indicated that the formation of protonated water cluster ions, $(\text{H}_2\text{O})_n\text{H}^+$, begins shortly downstream from the high-voltage pin electrode in the active discharge region. Subsequently, the $(\text{H}_2\text{O})_n\text{H}^+$ ions grow in size as they flow with the He gas. The effect of N_2 and H_2O impurities in the He plasma gas, the relative

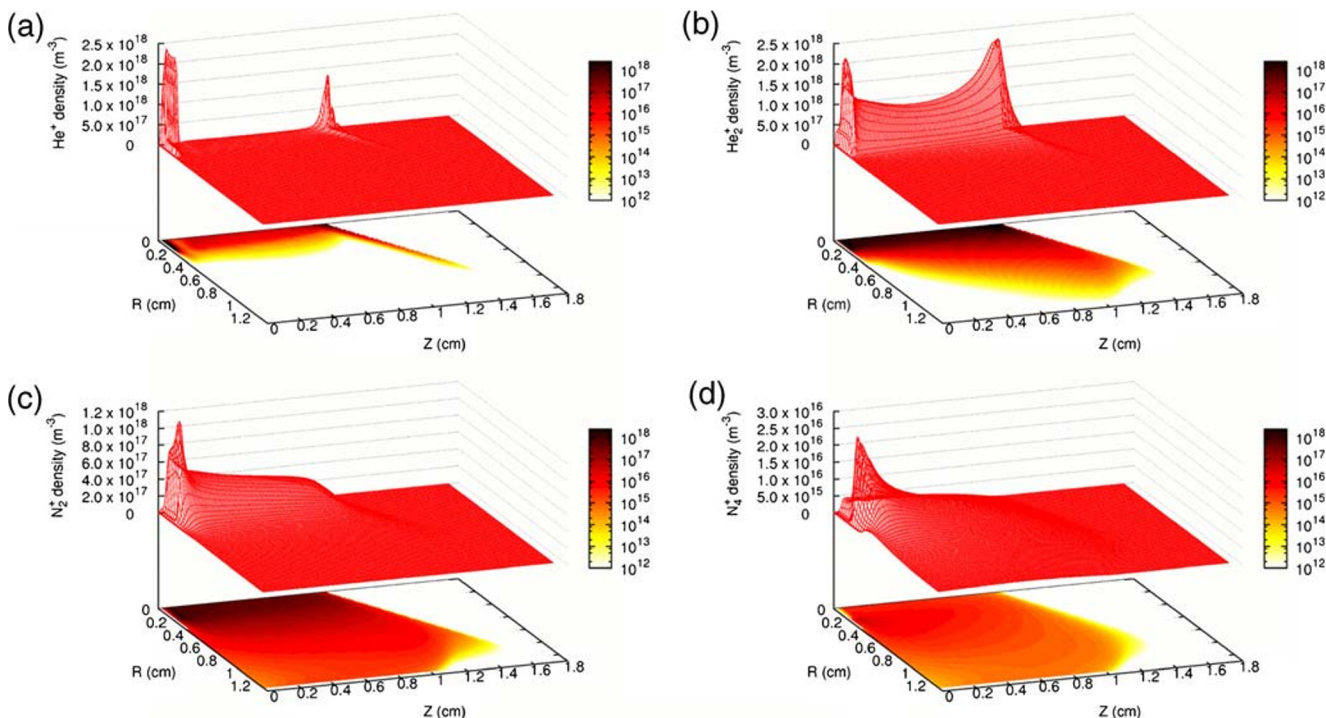


Fig. 17 Calculated 2D number density profiles of the He^+ (a), He_2^+ (b), N_2^+ (c), and N_4^+ (d) ions, in an APGD, operating at a He pressure of 1 atm with 10 ppm N_2 impurities, a DC voltage of 650 V, an electric current of

30 mA, and a gas temperature of 1350 K. Adopted from [121] with permission

humidity of the air around the discharge tube, and the air pressure was investigated. The impurity levels in the plasma gas were found to have the largest effect on the formation of water clusters.

These modeling efforts are very valuable, but in fact, they are only first attempts to fully understand atmospheric pressure NTP sources for analytical chemistry. Further insights into the analytical performance of these sources must be obtained from more extensive modeling. Just like for the other plasma sources described in this feature article, useful input can be obtained from modeling of atmospheric pressure NTPs used for other applications than in analytical chemistry.

Indeed, DBDs are among the most popular atmospheric pressure NTPs, used for many applications, including coating deposition (e.g., polymer coatings, plasma polymerization,...), plasma display panels, ozone synthesis, air pollution control, CO₂ conversion into value-added compounds, and even in plasma medicine [124, 125]. In addition, corona discharges, APGDs, and plasma jets are also used for many of these applications [125]. Note that plasma jets are often created from DBDs with fast gas flow, so that a plume is formed, hence showing quite some similarities with the flowing atmospheric pressure afterglow (FAPA) used in analytical chemistry.

Several models have been developed in the past for DBDs, APGDs, and plasma jets, to improve the various environmental, medical, and materials applications of this type of plasmas (e.g., [126–142]). As explained above, because of the atmospheric pressure operation, fluid models (typically in 1D or

2D), as well as 0D chemical kinetics models, are most common (see advantages and limitations of the various models in “Modeling approaches” in “Modeling of glow discharges”). 0D chemical kinetics models focus on the detailed plasma chemistry, which can indeed be very extensive in atmospheric pressure plasmas, as they typically operate in air or other molecular gas mixtures. Fluid models, on the other hand, focus more on the source design, typically with somewhat more limited chemistry, because of calculation time. It is obvious that similar methodologies can also be applied for modeling atmospheric pressure NTPs, used as ambient desorption/ionization plasma sources in analytical chemistry.

For instance, Fig. 18 illustrates an Ar plasma jet (top panel), as used in plasma medicine (e.g., for sterilization, wound treatment, and cancer treatment), consisting of a tip needle electrode, where the plasma is created, which is blown to the nozzle exit, due to the gas flow, forming a plume or so-called flowing afterglow. This plasma jet was modeled in [140] with a 0D chemical kinetics model. As explained in “Modeling approaches” in “Modeling of glow discharges,” this model only calculates the plasma characteristics as a function of time, assuming a homogeneous plasma volume, but in fact, this plasma volume moves as a function of distance, away from the tip needle electrode, due to the gas flow. Hence, the time dependence of the plasma characteristics, as calculated by the model, can be translated into a spatial dependence (as a function of distance from the tip needle electrode or nozzle exit), based on the gas flow velocity. This is illustrated in Fig. 18 (lower panel), showing the time and

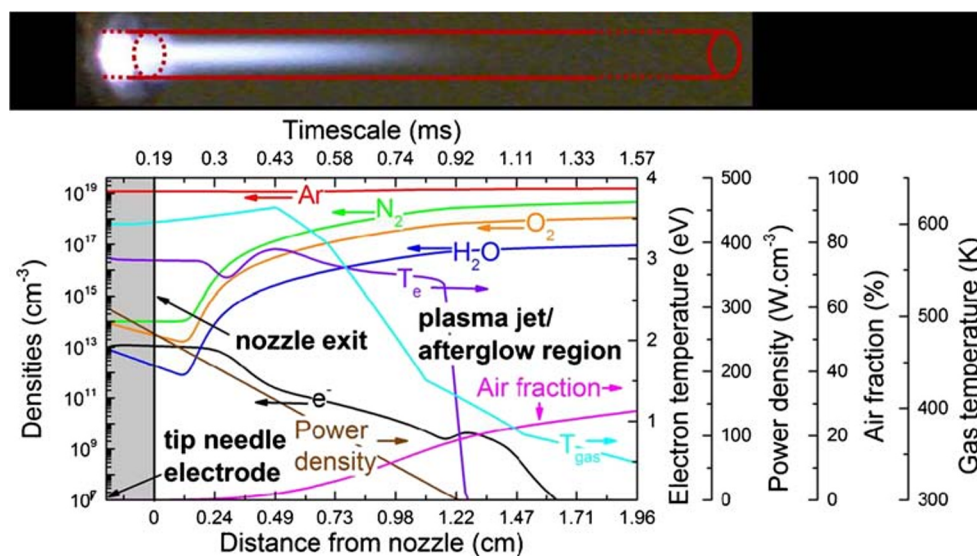


Fig. 18 Plasma characteristics as a function of distance from the nozzle exit of an Ar plasma jet, flowing into ambient air. The Ar flow rate is 2 L/min, adopted from the experiments, and contains 10 ppm N₂/O₂ and 1 ppm H₂O as impurities. The ambient air has a relative humidity of 50%. The temperature at the tip of the needle electrode is 600 K, and the total deposited power, adopted from the experiments, is 6.5 W. The profiles shown in this figure for the power deposition, gas temperature,

and humid air densities/fractions in Ar due to diffusion were fitted to experimental values, whereas the average electron temperature (T_e) and electron density (e^-) were calculated in the model. The interior of the plasma jet device is represented by the gray area, beginning at the needle electrode tip. This zone ends at the nozzle exit (indicated with axial position = 0 cm) and is followed by the plasma jet/afterglow region. Adopted from [140] with permission

spatial dependence (top and bottom x-axes) of various gas and plasma characteristics, such as the Ar density, and the densities of N_2 , O_2 , and H_2O , when the Ar jet flows into ambient air, as well as the power density, gas temperature, electron temperature, and electron density.

Figure 19 shows the calculated densities of all species in the same plasma jet as in Fig. 18, as a function of distance from the nozzle exit along the symmetry axis of the plasma jet.

In Fig. 19, a distinction is made between Ar species (a), nitrogen species (b), oxygen species (c), water species (d), NOx species (e), and ionic water clusters (f). The figures show which species are important at which positions in the afterglow. More details can be found in [140]. As this plasma jet, and other plasma jet designs used in plasma medicine, show some resemblance to the FAPA source or other ambient/desorption ionization sources, the modeling and results

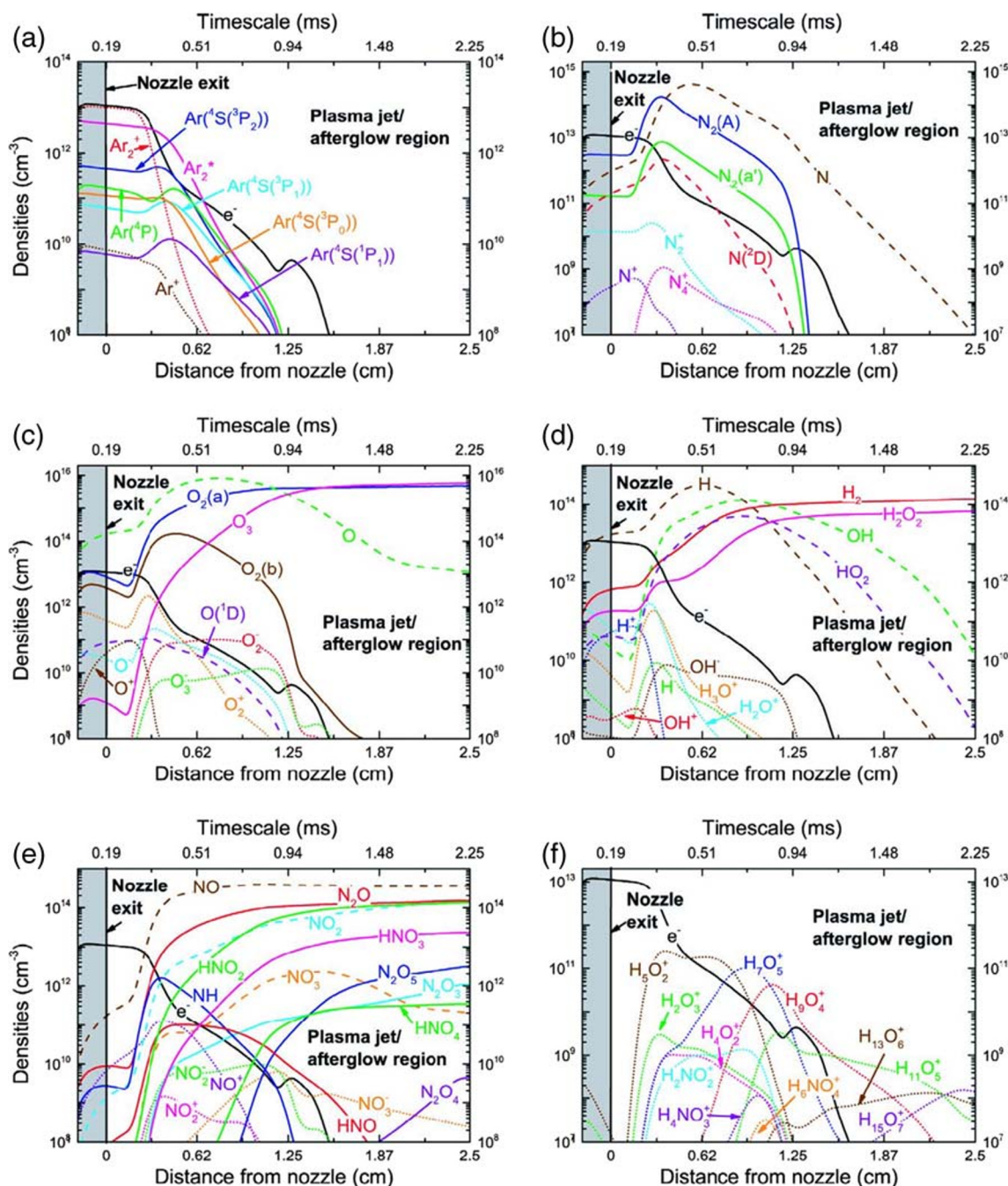


Fig. 19 Densities of various plasma species, along the symmetry axis of the plasma jet depicted in Fig. 18: (a) Ar species, (b) nitrogen species, (c) oxygen species, (d) water species, (e) NOx species, and (f) ionic water clusters. Molecules are indicated by a solid line, radicals by a dashed line

and ions by a dotted line. The timescale and distance from the nozzle (top and bottom x-axes) are correlated by the gas flow velocity profile. The conditions are the same as in Fig. 18. Adopted from [140] with permission

obtained for these plasma jet designs can also be very insightful for analytical chemistry sources.

Finally, besides atmospheric pressure NTPs for gaseous sampling, there is also a lot of interest in plasmas with liquid sampling for analytical chemistry purposes, such as the solution-cathode glow discharge (SCGD) [19, 20] and the liquid sampling atmospheric pressure glow discharge (LS-APGD) [21]. Also here, much information can be gained from models developed for other plasma applications. Indeed, plasma–liquid interaction is extremely important for many interesting applications, like water treatment, pollution control in various liquids, nanomaterial synthesis, plasma medicine, high-voltage switching, etc. However, the underlying mechanisms are very complicated and require detailed modeling [143, 144]. To obtain better insights and improve the above applications (mainly for plasma medicine), several models have been developed for plasma–liquid interaction, focusing among others on gas and liquid flow dynamics, as well as gas-phase and liquid-phase chemistry (e.g., [145–154]). The most appropriate models in this case are again fluid models (with focus on the gas and liquid flow dynamics) or 0D chemical kinetics models (focusing on detailed chemistry in both gas and liquid phase).

As an illustration, Fig. 20c shows calculated flow profiles in both gas and liquid phase, obtained from 2D fluid dynamics simulations [154], for a (so-called kINPen) plasma jet interacting with water, contained in a well of 2 mL, at a flow rate of 3 slm Ar (see Fig. 20a, b). The gas flows through the device, towards the liquid, and when it reaches the liquid

surface, it flows towards the edge of the well, causing a shear stress on the liquid surface. Upon hitting the edge of the well, the gas flow results in a vortex within the well, so that the gas flows back towards the afterglow. Because of the shear stress on the liquid surface, the upper layer of the liquid starts to move in the same direction as the gas, but with a lower velocity. The liquid movement results in another vortex in the liquid phase (see close-up in Fig. 20c).

The gas-phase densities and liquid-phase concentrations of all species can also be calculated with such a model, and details can be found, e.g., in [154]. This yields information on the major species in both gas and liquid phases. In addition, information can be provided on how these species are formed and converted into each other, as illustrated in Fig. 21, for the liquid phase of the plasma jet shown in Fig. 20.

In this case, i.e., Ar plasma jet flowing into ambient air, in contact with liquid water, the major species in the liquid are H_2O_2 , HNO_2 , and HNO_3 (indicated with blue background and black frames in Fig. 21). Their liquid-phase chemistry is mainly driven by reactions of short-lived species (indicated with white background in Fig. 21), like OH and NO_2 , and more specifically in the first few nm below the gas–liquid interface, where these short-lived species are still present (because they cannot survive deeper in the liquid, due to their high reactivity). ONOOH , HO_2 , and O_3 (indicated with blue background but without black frames in Fig. 21) are able to accumulate to some extent in the liquid during plasma treatment, but their concentrations clearly drop after plasma treatment. This can be either due to loss by chemical reactions (i.e., for ONOOH

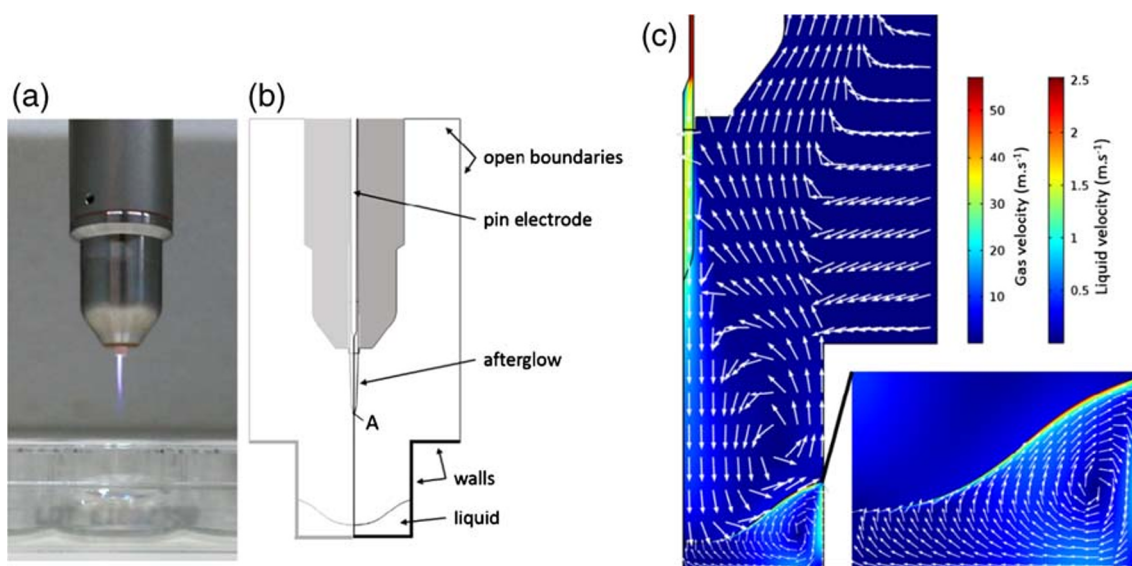
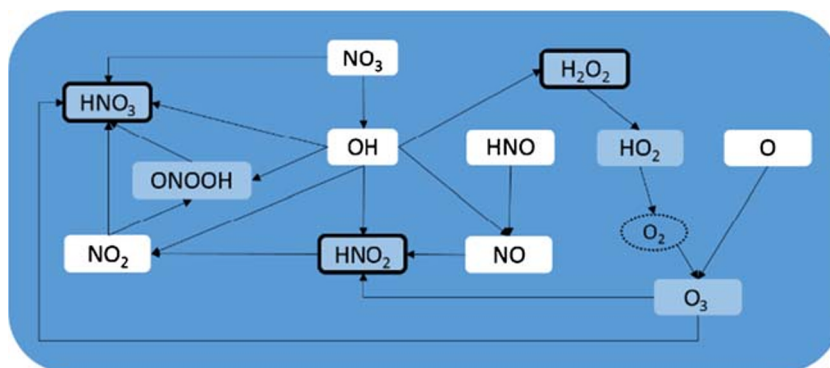


Fig. 20 **a** Picture of the kINPen® plasma jet while treating 2 mL of liquid in a well of a 12-well plate with 3 slm of Ar. **b** Geometry of the simulated system in a 2D fluid dynamics model based on the picture in (a). The right part in (b) forms the axisymmetric geometry described in the model, while the left part is added to form the full 2D geometry. **c** Calculated gas and liquid flow profiles, for an initial temperature of the gas and liquid phase of 295 K. According to experiments, the gas temperature in the

kINPen® source is 327 K, thus both the inflowing gas and the inside walls of the plasma jet are set to 327 K. The ambient air is 78.09% N_2 , 20.95% O_2 , and 0.96% H_2O , with a pressure of 1 atm. The liquid is defined as buffered water, with a pH of 7.3. The color scale gives the velocity magnitudes, while the arrows show the flow direction. Adopted from [154]—reproduced by permission of the PCCP Owner Societies

Fig. 21 Schematic overview of the important species produced in liquid water, upon interaction with an Ar plasma jet flowing in ambient air, and how they are converted into each other (see text)



and HO_2), or due to evaporation into the gas phase (as is the case for O_3 , because of its low Henry's constant).

This example originates from plasma-treated liquids used in plasma medicine, but it illustrates how these modeling efforts could also be very useful for a better understanding of liquid sampling plasmas in analytical chemistry.

Conclusion

Various types of plasmas are used in analytical chemistry, such as inductively coupled plasmas (ICPs) and glow discharges (GDs), used in combination with mass spectrometry (MS) or optical emission spectrometry (OES), as well as laser ablation (LA) for sample introduction in the ICP and for laser-induced breakdown spectroscopy (LIBS). To improve these applications, a good insight into the underlying plasma mechanisms is crucial. This insight can partially be obtained by experiments, but measurements inside the plasma are not always straightforward and often disturb the plasma characteristics. Therefore, computer modeling can also be very useful, as it can describe in detail the behavior of the various plasma species.

In the past 25 years, we developed various models for the abovementioned plasmas used in analytical chemistry. In this review paper, these modeling approaches are briefly presented. They are different for each case (e.g., depending on whether the plasma is in LTE or not, and whether gas flow dynamics is important or not). In addition, some characteristic results are shown, of interest for the application, such as crater profiles and optical emission spectra obtained in a GD, plasma temperature, electron density, gas flow path lines, evaporation of sample particles, and species density profiles in the ICP, temperature distributions inside a target material, melt and evaporation depth, and density profiles, velocity, and temperature distributions in the plume in case of LA and LIBS, as well as gas flow behavior in LA cells. Overall, these examples of typical calculation results illustrate that a lot of information can be obtained from modeling, which is sometimes not

possible or difficult to obtain from experiments. Hence, modeling can be useful to gain more insight to improve the applications.

It is important to note that the above plasmas are not only used in analytical chemistry, but also in other applications, for which similar models have been developed. When developing our models, we learned a lot from the models developed in these other fields.

The same is now applicable to novel types of plasmas that are gaining increasing interest for analytical chemistry, including various plasma sources used for gaseous sampling, in e.g., ambient desorption/ionization mass spectrometry, such as DBDs, APGDs, and plasma jets, as well as plasma sources for liquid sampling. Indeed, there is nowadays significant interest in DBDs, APGDs, and plasma jets, as well as in plasma-liquid interaction, for various environmental, medical, and materials applications. Various models are now being developed for these types of plasmas, and such efforts could be very helpful for developing models for the various novel analytical plasma sources as well, as illustrated in the last section with a few examples. In conclusion, this demonstrates that cross-fertilization from other fields is in general of great value in scientific research.

Acknowledgments M. Aghaei, Z. Chen, D. Autrique, T. Martens, and P. Heirman are gratefully acknowledged for their valuable efforts in the model developments illustrated in this paper.

Compliance with ethical standards

Conflict of interest The author declares that there is no conflict of interest.

References

1. Montaser A. Inductively coupled plasma mass spectrometry. New York: Wiley; 1992.
2. Montaser A. Inductively coupled plasma mass spectrometry. New York: Wiley; 1998.
3. Houk RS, Fassel VA, Flesch GD, Svec HJ, Gray AL, Taylor CE. Inductively coupled argon plasma as an ion source for mass

- spectrometric determination of trace elements. *Anal Chem.* 1980;52:2283–9.
4. Russo RE. Laser ablation. *Appl Spectrosc.* 1995;49:14A–28A.
 5. Günther D, Jackson SE, Longerich HP. Laser ablation and arc/spark solid sample introduction into inductively coupled plasma mass spectrometers. *Spectrochim Acta Part B.* 1999;54:381–409.
 6. Russo RE, Mao X, Mao SS. The physics of laser ablation in microchemical analysis. *Anal Chem.* 2002;74:70A–7A.
 7. Hattendorf B, Latkoczy C, Günther D. Laser ablation inductively coupled plasma mass spectrometry - it's the aerosol size that really matters in this high-throughput technique for ultratrace analysis of solids. *Anal Chem.* 2003;75:341A–7A.
 8. Radziemski LJ. From LASER to LIBS, the path of technology development. *Spectrochim. Acta Part B.* 2002;57:1109–13.
 9. Cristoforetti G, De Giacomo A, Dell'Aglio M, Legnaioli S, Tognoni E, Palleschi V, et al. Views and criticism: local thermodynamic equilibrium in laser-induced breakdown spectroscopy: beyond the McWhirter criterion. *Spectrochim Acta Part B.* 2010;65:86–95.
 10. De Giacomo A, Gaudiuso R, Koral C, Dell'Aglio M, De Pascale O. Nanoparticle enhanced laser induced breakdown spectroscopy: effect of nanoparticles deposited on sample surface on laser ablation and plasma emission. *Spectrochim Acta B.* 2014;98:19–27.
 11. Harrison WW, Hess KR, Marcus RK, King FL. Glow discharge mass spectrometry. *Anal Chem.* 1986;58:341A–56A.
 12. Hang W, Walden WO, Harrison WW. Microsecond pulsed glow discharge as an analytical spectroscopic source. *Anal Chem.* 1996;68:1148–52.
 13. Lobo L, Tuccitto N, Bordel N, Pereiro R, Pisonero J, Licciardello A, et al. Polymer screening by radiofrequency glow discharge time-of-flight mass spectrometry. *Anal Bioanal Chem.* 2010;396:2863–9.
 14. Bengtson A. A contribution to the solution of the problem of quantification in surface analysis work using glow discharge atomic emission spectroscopy. *Spectrochim Acta Part B.* 1985;40:631–9.
 15. Smoluch M, Mielczarek P, Silberring J. Plasma-based ambient ionization mass spectrometry in bioanalytical sciences. *Mass Spectrom Rev.* 2016;35:22–34.
 16. Badal SP, Michalak SD, Chan GC-Y, You Y, Shelley JT. Tunable ionization modes of a flowing atmospheric-pressure afterglow (FAPA) ambient ionization source. *Anal Chem.* 2016;88:3494–503.
 17. Andrade FJ, Shelley T, Wetzel WC, Webb MR, Gamez G, Ray SJ, et al. Atmospheric pressure chemical ionization source. 1. Ionization of compounds in the gas phase. *Anal Chem.* 2008;80:2646–53.
 18. Shelley JT, Hieftje GM. Ionization matrix effects in plasma-based ambient mass spectrometry sources. *J Anal Atom Spectrom.* 2010;25:345–50.
 19. Schwartz AJ, Shelley JT, Walton CL, Williams KL, Hieftje GM. Atmospheric-pressure ionization and fragmentation of peptides by solution-cathode glow discharge. *Chem Sci.* 2016;7:6440–9.
 20. Decker CG, Webb MR. Measurement of sample and plasma properties in solution-cathode glow discharge and effects of organic additives on these properties. *J Anal Atom Spectrom.* 2016;31:311–8.
 21. Hoegg ED, Barinaga CJ, Hager GJ, Hart GL, Koppelaar DW, Marcus RK. Preliminary figures of merit for isotope ratio measurements: the liquid sampling-atmospheric pressure glow discharge microplasma ionization source coupled to an Orbitrap mass analyzer. *J Amer Soc Mass Spectrom.* 2016;27:1393–403.
 22. Bogaerts A, van Straaten M, Gijbels R. Monte Carlo simulation of an analytical glow discharge: motion of electrons, ions and fast neutrals in the cathode dark space. *Spectrochim Acta Part B.* 1995;50:179–96.
 23. Bogaerts A, Gijbels R, Goedheer WJ. Hybrid Monte Carlo-fluid model of a direct current glow discharge. *J Appl Phys.* 1995;78:2233–41.
 24. Bogaerts A, Gijbels R. The role of fast argon ions and atoms in the ionization of argon in a direct current glow discharge: a mathematical simulation. *J Appl Phys.* 1995;78:6427–31.
 25. Bogaerts A, Gijbels R, Goedheer WJ. Two-dimensional model of a direct current glow discharge: description of the electrons, argon ions and fast argon atoms. *Anal Chem.* 1996;68:2296–303.
 26. Passchier JDP, Goedheer WJ. Relaxation phenomena after laser-induced photodetachment in electronegative rf discharges. *J Appl Phys.* 1993;73:1073–9.
 27. Boeuf JP. Numerical model of rf glow discharges. *Phys. Rev.* 1987;A36:2782–92.
 28. Graves DB, Jensen KF. A continuum model of DC and RF discharges. *IEEE trans. Plasma Sci.* 1986;14:78–91.
 29. Meyyappan M, Kreskovsky JP. Glow discharge simulation through solutions to the moments of the Boltzmann transport equation. *J Appl Phys.* 1990;68:1506–12.
 30. Bradley JW. A fluid model of the edge plasma in low-temperature discharges containing beam electrons. *J Phys D Appl Phys.* 1996;29:706–15.
 31. Carman RJ, Maitland A. A simulation of electron motion in the cathode sheath region of a glow discharge in helium. *J Phys D Appl Phys.* 1987;20:1021–30.
 32. Carman RJ. A simulation of electron motion in the cathode sheath region of a glow discharge in argon. *J Phys D Appl Phys.* 1989;22:55–66.
 33. An TN, Marode E, Johnson PC. Monte Carlo simulation of electrons within the cathode fall of a glow discharge in helium. *J Phys D Appl Phys.* 1977;10:2317–28.
 34. Weng Y, Kushner M. Method for including electron-electron collisions in Monte Carlo simulations of electron swarms in partially ionized gases. *Phys Rev A.* 1990;42:6192–200.
 35. Donko Z, Rozsa K, Tobin RC. Monte Carlo analysis of the electrons' motion in a segmented hollow cathode discharge. *J Phys D Appl Phys.* 1996;29:105–14.
 36. Helin W, Zuli L, Daming L, Boming Y. Electron energy and angular distribution of electrons in a helium DC glow discharge cathode sheath with transverse magnetic fields. *Vacuum.* 1996;47:167–72.
 37. Surendra M, Graves DB, Jellum GM. Self-consistent model of a direct-current glow discharge: treatment of fast electrons. *Phys Rev A.* 1990;41:1112–25.
 38. Sommerer TJ, Kushner MJ. Numerical investigation of the kinetics and chemistry of rf glow discharge plasmas sustained in He, N₂, O₂, He/N₂/O₂, He/CF₄/O₂, and SiH₄/NH₃ using a Monte Carlo-fluid hybrid model. *J Appl Phys.* 1992;71:1654–73.
 39. Huang FY, Kushner MJ. A hybrid model for particle transport and electron energy distributions in positive column electrical discharges using equivalent species transport. *J Appl Phys.* 1995;78:5909–18.
 40. Alves LL. Fluid modelling of the positive column of direct-current glow discharges. *Plasma Sources Sci Technol.* 2007;16:557–69.
 41. Salabas A, Gousset G, Alves LL. Two-dimensional fluid modelling of charged particle transport in radio-frequency capacitively coupled discharges. *Plasma Sources Sci Technol.* 2002;11:448–65.
 42. Alves LL, Gousset G, Vallée S. Nonequilibrium positive column revisited. *IEEE Trans. Plasma Sci.* 2003;31:572–86.
 43. Bogaerts A, van Straaten M, Gijbels R. Description of the thermalization process of the sputtered atoms in a glow discharge, using a three-dimensional Monte Carlo method. *J Appl Phys.* 1995;77:1868–74.

44. Bogaerts A, Gijbels R. Role of sputtered Cu atoms and ions in a direct current glow discharge: combined fluid and Monte Carlo model. *J Appl Phys*. 1996;79:1279–86.
45. Bogaerts A, Gijbels R. Modeling of metastable argon atoms in a direct current glow discharge. *Phys Rev A*. 1995;52:3743–51.
46. Bogaerts A, Gijbels R. Two-dimensional model of a direct current glow discharge: description of the argon metastable atoms, sputtered atoms and ions. *Anal Chem*. 1996;68:2676–85.
47. Bogaerts A, Gijbels R, Vlcek J. Collisional-radiative model for an argon glow discharge. *J Appl Phys*. 1998;84:121–36.
48. Bogaerts A, Gijbels R, Carman RJ. Collisional-radiative model for the sputtered copper atoms and ions in a direct current argon glow discharge. *Spectrochim Acta Part B*. 1998;53:1679–703.
49. Vlcek J. A collisional-radiative model applicable to argon discharges over a wide range of conditions. I. Formulation and basic data. *J Phys D Appl Phys*. 1989;22:623–31.
50. Carman RJ, Brown DJW, Piper JA. A self-consistent model for the discharge kinetics in a high-repetition-rate copper-vapor laser. *IEEE J Quant Electron*. 1994;30:1876–95.
51. Bogaerts A, Gijbels R. Modeling of glow discharges: what can we learn from it? *Anal Chem*. 1997;69:A719–27.
52. Bogaerts A, Gijbels R. Comprehensive description of a Grimm-type glow discharge source used for optical emission spectrometry: a mathematical simulation. *Spectrochim Acta Part B*. 1998;53:437–62.
53. Bogaerts A, Wagner E, Smith BW, Winefordner JD, Pollmann D, Harrison WW, et al. Three-dimensional density profiles of sputtered atoms and ions in a direct current glow discharge: experimental study and comparison with calculations. *Spectrochim Acta Part B*. 1997;52:205–18.
54. Bogaerts A, Guenard RD, Smith BW, Winefordner JD, Harrison WW, Gijbels R. Three-dimensional density profiles of the argon metastable atoms in a direct current glow discharge: experimental study and comparison with calculations. *Spectrochim Acta Part B*. 1997;52:219–29.
55. Bogaerts A, Gijbels R. Calculation of crater profiles on a flat cathode in a direct current glow discharge, and comparison with experiment. *Spectrochim Acta Part B*. 1997;52:765–78.
56. Bogaerts A, Verscharen W, Steers E. Computer simulations of crater profiles in GD-OES: comparison with experiments and investigation of the underlying mechanisms. *Spectrochim Acta Part B*. 2004;59:1403–11.
57. Bogaerts A, Gijbels R, Vlcek J. Modeling of glow discharge optical emission spectrometry: calculation of the argon atomic optical emission spectrum. *Spectrochim Acta Part B*. 1998;53:1517–26.
58. Bogaerts A, Gijbels R. Argon and copper optical emission spectra in a Grimm glow discharge source: mathematical simulations and comparison with experiment. *J Anal Atom Spectrom*. 1998;13:721–6.
59. Bogaerts A, Donko Z, Kutasi K, Bano G, Pinhao N, Pinheiro M. Comparison of calculated and measured optical emission intensities in a direct current argon-copper glow discharges. *Spectrochim Acta Part B*. 2000;55:1465–79.
60. Bogaerts A. Plasma diagnostics and numerical simulations: insight into the heart of analytical glow discharges. *J Anal Atom Spectrom*. 2007;22:13–40.
61. Bogaerts A, Wilken L, Hoffmann V, Gijbels R, Wetzig K. Comparison of modeling calculations with experimental results for direct current glow discharge optical emission spectrometry. *Spectrochim Acta Part B*. 2001;56:551–64.
62. Gamez G, Bogaerts A, Andrade F, Hieftje GM. Fundamental studies on a planar-cathode direct current glow discharge: part I. Characterization via laser scattering techniques. *Spectrochim Acta Part B*. 2004;59:435–47.
63. Bogaerts A, Gijbels R, Gamez G, Hieftje GM. Fundamental studies on a planar-cathode direct current glow discharge: part II. Numerical modeling and comparison with laser scattering experiments. *Spectrochim Acta Part B*. 2004;49:449–60.
64. Bogaerts A, Gijbels R, Goedheer WJ. Comparison between a radio-frequency and direct current glow discharge in argon by a hybrid Monte Carlo - fluid model for electrons, argon ions and fast argon atoms. *Spectrochim Acta Part B*. 1999;54:1335–50.
65. Bogaerts A, Gijbels R. Description of the argon excited levels in a radio-frequency and direct current glow discharge. *Spectrochim Acta Part B*. 2000;55:263–78.
66. Bogaerts A, Gijbels R. Behavior of the sputtered copper atoms, ions and excited species in a radio-frequency and direct current glow discharge. *Spectrochim Acta Part B*. 2000;55:279–97.
67. Bogaerts A, Gijbels R. Similarities and differences between direct current and radio-frequency glow discharges: a mathematical simulation. *J Anal Atom Spectrom*. 2000;15:1191–201.
68. Bogaerts A, Gijbels R, Goedheer W. Improved hybrid Monte Carlo - fluid model for the electrical characteristics in an analytical radio-frequency glow discharge in argon. *J Anal Atom Spectrom*. 2001;16:750–5.
69. Bogaerts A, Wilken L, Hoffmann V, Gijbels R, Wetzig K. Comparison of modeling calculations with experimental results for rf glow discharge optical emission spectrometry. *Spectrochim Acta Part B*. 2002;57:109–19.
70. Bogaerts A, Gijbels R. Hybrid Monte Carlo - fluid model for a microsecond pulsed glow discharge. *J Anal Atom Spectrom*. 2000;15:895–905.
71. Bogaerts A, Gijbels R. Modeling of a microsecond pulsed glow discharge: behavior of the argon excited levels and of the sputtered copper atoms and ions. *J Anal Atom Spectrom*. 2001;16:239–49.
72. Bogaerts A, Gijbels R, Jackson GP. Modeling of a millisecond pulsed glow discharge: investigation of the afterpeak. *J Anal Atom Spectrom*. 2003;18:533–48.
73. Bogaerts A. The afterglow mystery of pulsed glow discharges and the role of dissociative electron-ion recombination. *J Anal Atom Spectrom*. 2007;22:502–12.
74. Bogaerts A, Gijbels R, Serikov VV. Calculation of gas heating in direct current argon glow discharges. *J Appl Phys*. 2000;87:8334–44.
75. Bogaerts A, Okhrimovskyy A, Gijbels R. Calculation of the gas flow and its effect on the plasma characteristics for a modified Grimm-type glow discharge cell. *J Anal Atom Spectrom*. 2002;17:1076–82.
76. Bogaerts A, Gijbels R. Calculation of cathode heating in analytical glow discharges. *J Anal Atom Spectrom*. 2004;18:1206–12.
77. Bogaerts A, Gijbels R. Effects of adding hydrogen to an argon glow discharge: overview of relevant processes and some qualitative explanations. *J Anal Atom Spectrom*. 2000;15:441–9.
78. Bogaerts A, Gijbels R. Hybrid Monte Carlo - fluid modeling network for an argon/hydrogen direct current glow discharge. *Spectrochim Acta Part B*. 2002;57:1071–99.
79. Bogaerts A. Hydrogen addition to an argon glow discharge: a numerical simulation. *J Anal Atom Spectrom*. 2002;17:768–79.
80. Bogaerts A. Computer simulations of argon - hydrogen Grimm-type glow discharges. *J Anal Atom Spectrom*. 2008;23:1441–556.
81. Bogaerts A. Hybrid Monte Carlo - fluid model for studying the effects of nitrogen addition to argon glow discharges. *Spectrochim Acta Part B*. 2009;64:126–40.
82. Bogaerts A. Effects of oxygen addition to argon glow discharges: a hybrid Monte Carlo - fluid modeling investigation. *Spectrochim Acta Part B*. 2009;64:1266–79.
83. Bogaerts A, Gijbels R. Relative sensitivity factors in glow discharge mass spectrometry: the role of charge transfer ionization. *J Anal Atom Spectrom*. 1996;11:841–7.

84. Bogaerts A, Temelkov KA, Vuchkov NK, Gijbels R. Calculation of rate constants for asymmetric charge transfer, and their effect on relative sensitivity factors in glow discharge mass spectrometry. *Spectrochim Acta Part B*. 2007;62:325–36.
85. Lindner H, Bogaerts A. Multi-element model for the simulation of inductively coupled plasmas: effects of helium addition to the central gas stream. *Spectrochim Acta Part B*. 2001;66:421–31.
86. Lindner H, Murtazin A, Groh S, Niemax K, Bogaerts A. Simulation and experimental studies on plasma temperature, flow velocity and injector diameter effects for an inductively coupled plasma. *Anal Chem*. 2011;83:9260–6.
87. Aghaei M, Lindner H, Bogaerts A. Effect of a mass spectrometer interface on inductively coupled plasma characteristics: a computational study. *J Anal Atom Spectrom*. 2012;27:604–10.
88. Aghaei M, Lindner H, Bogaerts A. Optimization of operating parameters for inductively coupled plasma mass spectrometry: a computational study. *Spectrochim Acta Part B*. 2012;76:56–64.
89. Aghaei M, Lindner H, Bogaerts A. Effect of sampling cone position and diameter on the gas flow dynamics in an ICP. *J Anal Atom Spectrom*. 2013;28:1485–92.
90. Aghaei M, Flamigni L, Lindner H, Gunther D, Bogaerts A. Occurrence of gas flow rotational motion inside the ICP torch: a computational and experimental study. *J Anal Atom Spectrom*. 2014;29:249–61.
91. Aghaei M, Bogaerts A. Particle transport through an inductively coupled plasma torch: elemental droplet evaporation. *J Anal Atom Spectrom*. 2016;31:545–822.
92. Aghaei M, Lindner H, Bogaerts A. Ion clouds in the ICP torch: a closer look through computations. *Anal Chem*. 2016;88:8005–2018.
93. Bogaerts A, Aghaei M. Inductively coupled plasma – mass spectrometry: insights through computer modeling. *J Anal Atom Spectrom*. 2017;32:233–61.
94. Boulos MI. Heating of powders in the fire ball of an induction plasma. *IEEE Trans Plasma Sci*. 1978;6:91–106.
95. Mostaghimi J, Pfender E. Effects of metallic vapor on the properties of an argon arc plasma. *Plasma Chem Plasma Process*. 1984;4:199–217.
96. Mostaghimi J, Proulx P, Boulos MI, Barnes RM. Computer modeling of the emission patterns for a spectrochemical ICP. *Spectrochim Acta Part B*. 1985;40:153–66.
97. Zhao GY, Mostaghimi J, Boulos MI. The induction plasma chemical reactor: part I. Equilibrium model. *Plasma Chem Plasma Process*. 1990;10:133–50.
98. Zhao GY, Mostaghimi J, Boulos MI. The induction plasma chemical reactor: part II. Kinetic model. *Plasma Chem Plasma Process*. 1990;10:151–66.
99. Colombo V, Ghedini E, Sanibondi P. Three-dimensional investigation of particle treatment in an rf thermal plasma with reaction chamber. *Plasma Sources Sci Technol*. 2010;19:065024–36.
100. Colombo V, Ghedini E, Sanibondi P. Two-temperature thermodynamic and transport properties of argon-hydrogen and nitrogen-hydrogen plasmas. *J Phys D Appl Phys*. 2009;42:055213–24.
101. Colombo V, Ghedini E, Mostaghimi J. Three-dimensional modeling of an inductively coupled plasma torch for spectroscopic analysis. *IEEE Trans Plasma Sci*. 2008;36:1040–1.
102. Shigeta M. Three-dimensional flow dynamics of an argon rf plasma with dc jet assistance: a numerical study. *J Phys D Appl Phys*. 2013;46:015401–13.
103. Shigeta M. Time-dependent 3D simulation of an argon rf inductively coupled thermal plasma. *Plasma Sources Sci Technol*. 2012;21:055029–43.
104. Shigeta M, Watanabe T. Numerical investigation of cooling effect on platinum nanoparticle formation in inductively coupled thermal plasmas. *J Appl Phys*. 2008;103:074903–18.
105. Bogaerts A, Chen Z, Gijbels R, Vertes A. Laser ablation for analytical sampling: what can we learn from modeling? *Spectrochim Acta Part B*. 2003;58:1867–93.
106. Chen Z, Bogaerts A. Laser ablation of Cu and plume expansion into 1 atm ambient gas. *J Appl Phys*. 2005;97:063305.
107. Bogaerts A, Chen Z. Nanosecond laser ablation of Cu: modeling of the expansion in He background gas, and comparison with the expansion in vacuum. *J Anal Atom Spectrom*. 2004;18:1169–76.
108. Bleiner D, Bogaerts A. Computer simulations of laser ablation sample introduction for plasma-source elemental microanalysis. *J Anal Atom Spectrom*. 2006;21:1161–74.
109. Bleiner D, Bogaerts A. Computer simulations of sample chambers for laser ablation - inductively coupled plasma mass spectrometry. *Spectrochim Acta Part B*. 2007;62:155–68.
110. Autrique D, Bogaerts A, Lindner H, Garcia CC, Niemax K. Design analysis of a laser ablation cell for inductively coupled plasma mass spectrometry by numerical simulation. *Spectrochim Acta Part B*. 2008;63:257–70.
111. Lindner H, Autrique D, Garcia CC, Niemax K, Bogaerts A. Optimized transport setup for high repetition rate pulse-separated analysis in laser ablation inductively coupled plasma mass spectrometry. *Anal Chem*. 2009;81:4241–8.
112. Lindner H, Autrique D, Pisonero J, Günther D, Bogaerts A. Numerical simulation analysis of flow patterns and particle transport in the HEAD laser ablation cell with respect to inductively coupled plasma spectrometry. *J Anal Atom Spectrom*. 2010;25:295–304.
113. Ready JF. Effects of high power laser radiation. New York: Academic Press; 1971.
114. Bogaerts A, Chen Z. Effect of laser parameters on laser ablation and laser-induced plasma formation: a numerical modelling investigation. *Spectrochim Acta Part B*. 2005;60:1280–307.
115. Bogaerts A, Chen Z, Bleiner D. Laser ablation of copper in different background gases: comparative study by numerical modeling and experiments. *J Anal Atom Spectrom*. 2006;21:384–95.
116. Chen Z, Bleiner D, Bogaerts A. Effect of ambient pressure on laser ablation and plume expansion dynamics: a numerical simulation. *J Appl Phys*. 2006;99:063304.
117. Bleiner D, Chen Z, Autrique D, Bogaerts A. Role of laser-induced melting and vaporization of metals during ICP-MS and LIBS analysis, investigated by computer simulations and experiments. *J Anal Atom Spectrom*. 2006;21:910–21.
118. Bogaerts A, Chen Z, Autrique D. Double pulse laser ablation and laser induced breakdown spectroscopy: a modeling investigation. *Spectrochim Acta Part B*. 2008;63:746–54.
119. Martens T, Bogaerts A, Brok W, van Dijk J. Computer simulations of a dielectric barrier discharge used for analytical spectrometry. *Anal Bioanal Chem*. 2007;388:1583–94.
120. Martens T, Bogaerts A, Brok WJM, van der Mullen JJAM. Modeling study on the influence of the pressure on a dielectric barrier discharge microplasma. *J. Anal. Atom. Spectrom*. 2007;22:1033–42.
121. Martens T, Mihailova D, van Dijk J, Bogaerts A. Theoretical characterization of an atmospheric pressure glow discharge used for analytical spectrometry. *Anal Chem*. 2009;81:9096–108.
122. Andrade FJ, Wetzel WC, Chan GC-Y, Webb MR, Gamez G, Ray SJ, et al. A new, versatile, direct-current helium atmospheric-pressure glow discharge. *J Anal Atom Spectrom*. 2006;21:1175–84.
123. Ellis WC, Spencer RL, Reininger C, Farnsworth PB. Computational model of a direct current glow discharge used as an ambient desorption/ionization source for mass spectrometry. *J Anal Atom Spectrom*. 2017;32:2407–15.
124. Kogelschatz U. Dielectric-barrier discharges: their history, discharge physics, and industrial applications. *Plasma Chem Plasma Process*. 2003;23:1–46.

125. Bogaerts A, Neyts E, Gijbels R, van der Mullen JJAM. Gas discharge plasmas and their applications. *Spectrochim Acta Part B*. 2002;57:609–58.
126. Eliasson B, Hirth M, Kogelschatz U. Ozone synthesis from oxygen in dielectric barrier discharges. *J Phys D Appl Phys*. 1987;20:1421–37.
127. Golubovskii Yu B, Maiorov VA, Behnke JF. Influence of interaction between charged particles and dielectric surface over a homogeneous barrier discharge in nitrogen. *J Phys D Appl Phys*. 2002;35:751–61.
128. Choi YH, Kim JH, Hwang YS. One-dimensional discharge simulation of nitrogen DBD atmospheric pressure plasma. *Thin Solid Films*. 2006;506–507:389–95.
129. Petrovic D, Martens T, van Dijk J, Brok WJM, Bogaerts A. Fluid modelling of an atmospheric pressure dielectric barrier discharge in cylindrical geometry. *J Phys D Appl Phys*. 2009;42:205206.
130. Lin K-M, Hu M-H, Hung C-T, Wu J-S, Hwang F-N, Chen Y-S, et al. A parallel hybrid numerical algorithm for simulating gas flow and gas discharge of an atmospheric-pressure plasma jet. *Comput Phys Commun*. 2012;183:2550–60.
131. Duan X, He F, Ouyang J. Uniformity of a dielectric barrier glow discharge: experiments and two-dimensional modeling. *Plasma Sources Sci Technol*. 2012;21:015008.
132. Van Laer K, Bogaerts A. Fluid modeling of a packed bed dielectric barrier discharge plasma reactor. *Plasma Sources Sci Technol*. 2016;25:015002.
133. Kruszelnicki J, Engeling KW, Foster JE, Xiong Z, Kushner MJ. Propagation of negative electric discharges through 2-dimensional packed bed reactors. *J Phys D Appl Phys*. 2017;50:025203.
134. Baliab N, Aggelopoulou CA, Skourasa ED, Tsakiroglou CD, Burganos VN. Modeling of a DBD plasma reactor for porous soil remediation. *Chem Eng J*. 2019;373:393–405.
135. Saridj A, Belarbi AW. Numerical modeling of a DBD in glow mode at atmospheric pressure. *J Theor Appl Phys*. 2019;13:179–90.
136. Trenchev G, Nikiforov A, Wang W, Kolev S, Bogaerts A. Atmospheric pressure glow discharge for CO₂ conversion: model-based exploration of the optimum reactor configuration. *Chem Eng J*. 2019;362:830–41.
137. Waskoenig J, Niemi K, Knake N, Graham LM, Reuter S, Schulz von der Gathen V, et al. Atomic oxygen formation in a radio-frequency driven micro-atmospheric pressure plasma jet. *Plasma Sources Sci Technol*. 2010;19:045018.
138. Murakami T, Niemi K, Gans T, O'Connell D, Graham WG. Afterglow chemistry of atmospheric-pressure helium-oxygen plasmas with humid air impurity. *Plasma Sources Sci Technol*. 2014;23:025005.
139. Sakiyama Y, Graves DB. Finite element analysis of an atmospheric pressure RF-excited plasma needle. *J Phys D Appl Phys*. 2006;39:3451–6.
140. Van Gaens W, Bogaerts A. Kinetic modelling for an atmospheric pressure argon plasma jet in humid air. *J Phys D Appl Phys*. 2013;46:275201.
141. Schmidt-Bleker A, Winter J, Iseni S, Dünbier M, Weltmann KD, Reuter S. Reactive species output of a plasma jet with a shielding gas device - combination of FTIR absorption spectroscopy and gas phase modelling. *J Phys D Appl Phys*. 2014;47:145201.
142. Lietz AM, Kushner MJ. Molecular admixtures and impurities in atmospheric pressure plasma jets. *J Appl Phys*. 2018;124:153303.
143. Bruggeman PJ, Kushner MJ, Locke BR, Gardeniers JGE, Graham WG, Graves DB, et al. Plasma-liquid interactions: a review and roadmap. *Plasma Sources Sci Technol*. 2016;25:053002.
144. Vanraes P, Bogaerts A. Plasma physics of liquids - a focused review. *Appl Phys Rev*. 2018;5:031103.
145. Babaeva NY, Tian W, Kushner MJ. The interaction between plasma filaments in dielectric barrier discharges and liquid covered wounds: electric fields delivered to model platelets and cells. *J Phys D Appl Phys*. 2014;47:235201.
146. Chen C, Liu DX, Liu ZC, Yang AJ, Chen HL, Shama G, et al. A model of plasma-biofilm and plasma-tissue interactions at ambient pressure. *Plasma Chem Plasma Process*. 2014;34:403–41.
147. Tian W, Lietz AM, Kushner MJ. The consequences of air flow on the distribution of aqueous species during dielectric barrier discharge treatment of thin water layers. *Plasma Sources Sci Technol*. 2016;25:055020.
148. Tian W, Kushner MJ. Long-term effects of multiply pulsed dielectric barrier discharges in air on thin water layers over tissue: stationary and random streamers. *J Phys D Appl Phys*. 2015;48:494002.
149. Tian W, Kushner MJ. Influence of excitation pulse duration of dielectric barrier discharges on biomedical applications. *J Phys D Appl Phys*. 2014;47:165201.
150. Lietz AM, Kushner MJ. Air plasma treatment of liquid covered tissue: long timescale chemistry. *J Phys D Appl Phys*. 2016;49:425204.
151. Lindsay A, Anderson C, Slikboer E, Shannon S, Graves D. Momentum, heat, and neutral mass transport in convective atmospheric pressure plasma-liquid systems and implications for aqueous targets. *J Phys D Appl Phys*. 2015;48:424007.
152. Norberg SA, Parsey GM, Lietz AM, Johnsen E, Kushner MJ. Atmospheric pressure plasma jets onto a reactive water layer over tissue: pulse repetition rate as a control mechanism. *J Phys D Appl Phys*. 2019;52:015201.
153. Verlact CCW, Van Boxem W, Bogaerts A. Transport and accumulation of plasma generated species in aqueous solution. *Phys Chem Chem Phys*. 2018;20:6845–59.
154. Heirman P, Van Boxem W, Bogaerts A. Reactivity and stability of plasma-generated oxygen and nitrogen species in buffered water solution: a computational study. *Phys Chem Chem Phys*. 2019;21:12881–94.

Publisher's note Springer Nature remains neutral with regard to jurisdictional claims in published maps and institutional affiliations.